

VLTI/PIONIER imaging of post-AGB binaries

An INSPIRING hunt for inner rim substructures in circumbinary discs^{*,**}

T. De Prins^{1,2,3,***}, A. Corporaal⁴, J. Kluska¹, D. Kamath^{2,3}, H. Van Winckel¹, K. Andrych^{2,3}, J. Alcolea⁵,
N. Anugu⁶, J.-P. Berger⁷, V. Bujarrabal⁸, I. Gallardo Cava⁵, S. Kraus⁹, and H. Olofsson¹⁰

¹ Institute of Astronomy, KU Leuven, Celestijnenlaan 200D, 3001 Leuven, Belgium

² School of Mathematical and Physical Sciences, Macquarie University, Balaclava Road, Sydney, NSW 2109, Australia

³ Astrophysics and Space Technologies Research Centre, Macquarie University, Balaclava Road, Sydney, NSW 2109, Australia

⁴ European Southern Observatory, Alonso de Córdova 3107, Vitacura, Casilla 19001, Santiago, Chile

⁵ Observatorio Astronómico Nacional (OAN-IGN), Alfonso XII 3, 28014 Madrid, Spain

⁶ The CHARA Array of Georgia State University, Mount Wilson Observatory, Mount Wilson, CA 91023, USA

⁷ Univ. Grenoble Alpes, CNRS, IPAG, F-38000 Grenoble, France

⁸ Observatorio Astronómico Nacional (OAN-IGN), Apartado 112, 28803 Alcalá de Henares, Madrid, Spain

⁹ Department of Physics and Astronomy, University of Exeter, Stocker Road, Exeter EX4 4QL, UK

¹⁰ Department of Space, Earth and Environment, Chalmers University of Technology, Onsala Space Observatory, 43992 Onsala, Sweden

Received 09 December 2025 / Accepted 11 May 2029

ABSTRACT

Context. Post-asymptotic giant branch (post-AGB) binaries are surrounded by stable dusty discs. Despite extensive evidence for disc-binary interactions and complex morphologies, systematic studies of the inner disc rim morphology and dynamics are lacking.

Aims. We image the detailed inner rim morphology for a sample of ‘full’ post-AGB circumbinary discs observed using NIR interferometry. At resolutions down to $\sim 1\text{--}2$ mas (corresponding to $\sim 1\text{--}10$ AU), we aim to reveal potential substructures that may trace perturbations from the binary or embedded substellar companions, or that arise from hydrodynamical instabilities.

Methods. We developed a systematic image reconstruction workflow using the SPARCO approach together with the ORGANIC reconstruction algorithm. This was applied to VLTI/PIONIER data of eight diverse post-AGB binaries obtained within the INSPIRING ESO large programme, providing high-fidelity images of dust continuum emission at the inner rim. Extensive tests were applied to assess the robustness of the recovered image features.

Results. The dusty disc rim is well-resolved for all targets. Only one of the images can be fully accounted for by simple radiative transfer effects due to disc inclination, while in several others indications of potential substructures are detected. Strikingly, four exhibit robust azimuthal brightness enhancements at locations not expected from inclination effects alone. These can indicate strong radiative or dynamical responses to the binary, or vortices formed via hydrodynamical instabilities. One target – IW Car – displays an even more puzzling morphology, showing a single large-scale outer flux arc and several small-scale arcs closer to the binary, possibly revealing accretion streams onto the binary, a misaligned innermost disc, or a spiral feature located in the disc or in an outflow.

Conclusions. This work presents the first homogeneous interferometric imaging survey of the inner regions of post-AGB circumbinary discs, enabling direct comparison of inner rim morphologies across a representative sample. The inner disc regions are highly diverse and dynamic, harbouring a significant amount of substructure candidates. Multi-wavelength and time-series imaging will be essential in constraining the extent, motion and wavelength-dependence of these features, and uncover their physical origins.

Key words. stars: AGB and post-AGB – techniques: high angular resolution – techniques: interferometric – protoplanetary disks – binaries: general – circumstellar matter

1. Introduction

Dusty circumstellar discs are observed in systems at various phases of stellar evolution. One such type of system is the post-asymptotic giant branch (post-AGB) binary (for a recent review, see Van Winckel 2025, and references therein). The post-AGB phase represents a brief period of contraction after the envelope of a low-to-intermediate mass star has been stripped on the AGB. The star remains at a constant luminosity on the order of $\sim 10^3\text{--}10^4 L_{\odot}$ (Van Winckel 2003), heating up until it reaches

the white dwarf phase in $\sim 10^4\text{--}10^5$ yr (Bertolami 2016). A large subset of post-AGB systems – about one third – show spectral energy distributions (SEDs) with broad infrared (IR) excesses, indicative of stable dusty circumbinary discs (e.g. de Ruyter et al. 2006; Kamath et al. 2014, 2015; Kluska et al. 2022). The binarity of these disc sources has been confirmed through extensive radial velocity (RV) monitoring, showing that the companions are likely on the main sequence (Oomen et al. 2018). Due to the strong link between IR excess and binarity, it is thought that the disc is formed from envelope material ejected during a poorly understood phase of binary interaction on the AGB (Van Winckel 2019). Recently, Kluska et al. (2022) presented an SED catalogue of 85 systems, encompassing all disc-bearing Galactic

* Based on observations collected at the European Southern Observatory under ESO programme 1103.D-0797.

** The reconstructed images are available at the CDS

*** Corresponding author, toon.deprins@kuleuven.be

post-AGB binaries known up to that date. Based on these SEDs, the authors showed that the majority of the dust discs can be considered part of the 'full' disc category, defined as discs with inner rims close to the dust sublimation radius and a corresponding excess starting in the near-infrared (NIR). In addition, they also identified a sizeable population of 'transition' discs, typified by larger inner cavities (confirmed using optical interferometry by [Corporaal et al. 2023a](#)) and excess starting in the mid-infrared (MIR).

The stability of post-AGB circumbinary discs is confirmed through the detection of Keplerian velocity fields in single-dish and interferometric (sub-)mm observations of CO lines ([Bujarrabal et al. 2013a,b, 2015, 2017, 2018](#); [Gallardo Cava et al. 2021](#)), revealing gas discs with outer radii of $\sim 100 - 1000$ AU (angular sizes $\lesssim 1.5 - 2''$ at typical system distances of $\gtrsim 1$ kpc). IR spectroscopy, mm photometry and mm interferometry reveal significant silicate grain crystallinity and grain growth (e.g. [Gielen et al. 2008](#); [Sahai et al. 2011](#); [Sciicluna et al. 2020](#); [Bujarrabal et al. 2023](#)) – in some cases up to at least mm size – showing that dust processing has proceeded to an advanced stage. The hot inner disc rim, at a typical size of several AU ($\sim 1 - 10$ mas), has been resolved in thermal dust emission using optical interferometry (e.g. [Kluska et al. 2019](#)). The outer disc regions are instead resolved in scattered light using single-telescope adaptive optics imagers (e.g. [Andrych et al. 2023, 2025](#)). Together with extensive radiative transfer (RT) modelling of the inner rim from optical interferometric data ([Hillen et al. 2014, 2015](#); [Kluska et al. 2018](#); [Corporaal et al. 2023b](#)), these observations have generally shown that post-AGB circumbinary discs display high degrees of similarity to passively irradiated protoplanetary discs (PPDs) around young stellar objects (YSOs).

Post-AGB circumbinary discs are not isolated from the rest of their system. While the influence of the central binary on the circumbinary disc morphology remains poorly constrained, there is strong observational evidence that the disc significantly affects the central binary. First, systematic depletion of dust-forming elements in the post-AGB primary's atmosphere, a phenomenon called 'refractory depletion', can be explained through dust trapping and subsequent re-accretion of cleaned gas from the circumbinary disc (e.g. [Giridhar et al. 1998](#); [Van Winckel 2003](#); [Oomen et al. 2019](#); [Mohorian et al. 2024, 2025](#)). Second, spectroscopic time-series reveal strong blue-shifted absorption in the Balmer lines, caused by a magnetically launched jet from a circumcompanion accretion disc, which is itself likely fed by re-accretion from the larger circumbinary disc (e.g. [Gorlova et al. 2012](#); [Bollen et al. 2022](#); [Verhamme et al. 2024](#); [De Prins et al. 2024](#)). This circumcompanion disc can be detected as a point source in optical interferometric observations ([Hillen et al. 2016](#); [Anugu et al. 2023](#)). In addition, [Kluska et al. \(2022\)](#) and [Mohorian et al. \(2025\)](#) found a correlation between transition discs and refractory depletion strength, leading the former to suggest that giant planets may be carving the transition disc cavities – as has been similarly proposed for PPDs around YSOs (e.g. [Kama et al. 2015](#)) – and raise the possibility of second-generation planet formation. Together, these findings demonstrate that the inner regions of post-AGB circumbinary discs must be viewed as highly dynamic environments, shaped by ongoing interactions.

Given their general similarities, it is natural to compare post-AGB discs with their younger PPD counterparts. Around PPDs, high-resolution thermal (sub-)mm and optical scattered-light imaging has revealed a wealth of substructures – spirals, arcs, rings, gaps, shadows, and crescents (e.g. [Andrews et al. 2018](#); [Garufi et al. 2024](#)). These features have become central to studies of planet formation, as they are often interpreted as

signposts of embedded planets or as outcomes of instabilities that may themselves promote planet formation (for a detailed review, see [Bae et al. 2023](#)). Indeed, previous efforts to resolve the outer regions of 11 post-AGB circumbinary discs with scattered light imaging ([Ertel et al. 2019](#); [Andrych et al. 2023, 2024, 2025](#)) have also shown diverse potential substructures, including arc-, spiral- and ring-like features. Conversely, the detailed morphology and presence of substructures near the inner post-AGB disc rim, where the effects of the binary are expected to be strongest, have been investigated to a much lesser extent.

While the inner rim has been resolved for larger samples using optical interferometry, this was typically through sparse observations suitable only for limited geometric modelling ([Hillen et al. 2017](#); [Kluska et al. 2019](#); [Corporaal et al. 2023a](#)). Given the expected complexity of the inner disc, information is preferably extracted using image reconstruction instead. Indeed, non-parametric image reconstructions have proven to be a powerful tool to reveal unexpected features in the inner regions of various systems – including PPDs (e.g. [Kluska et al. 2016, 2020a](#); [Ibrahim et al. 2023](#); [Setterholm et al. 2025](#)), stellar outflows (e.g. [Weigelt et al. 2016](#); [Planquart et al. 2024](#)) and stellar surfaces (e.g. [Drevon et al. 2024](#)) – whose presence would often be hard to infer using parametrised geometric models. Imaging of post-AGB inner circumbinary disc rims has nevertheless been limited to only two single-object studies, targeting IRAS 08544-4431 and HD 101584 ([Hillen et al. 2016](#); [Kluska et al. 2020b](#)), respectively revealing a perturbed azimuthal brightness distribution and a secondary ring – the latter possibly marking a secondary condensation front in a disc wind. These findings clearly deviated from the classical view of a smooth, inclined circular rim centred on a single star, where the emission is simply expected to be brightest and symmetric along the far side of the projected rim due to self-shadowing of the near side (e.g. [Hoffmann et al. 2022](#)).

In this study, we aim to systematically investigate the morphological complexity of post-AGB circumbinary disc inner rims. To this end, we present the first systematic NIR interferometric imaging survey for a diverse sample of targets, using observations taken with VLTI/PIONIER. Probing thermal emission from the hot inner rim dust, we focus on the detection of any asymmetric features possibly indicative of substructures induced by the central binary, substellar companions, or hydrodynamical instabilities. The article is structured as follows. We describe our targets in Sect. 2 and the observations and data in Sect. 3. Our image reconstruction workflow is developed in Sect. 4, and then applied to our targets in Sect. 5, where we describe the detected features. During this, we take into account multiple tests meant to assess the reliability of the image features. The possible origins of the rim positions and detected features are discussed in Sect. 6. Finally, we summarise our results and present our conclusions in Sect. 7.

2. Target systems

In this study, we present NIR H band interferometric imaging observations of eight full disc post-AGB binaries. All observations were obtained within the 'INterferometric Survey of Post-AGB binaries Interacting with their RING' large programme at the European Southern Observatory (INSPIRING, ESO 1103.D-0797, PI: J. Kluska). The data were taken using the Precision Integrated-Optics Near-infrared Imaging Experiment (PIONIER, [Le Bouquin et al. 2011](#)), mounted on the Very Large Telescope Interferometer (VLTI, [Haguenauer et al. 2010](#)). The

Table 1: Properties of the target sample and their observations.

Name	IRAS ID	P_{orb} (d)	$a_1 \sin i_{\text{bin}}$ (AU)	$f(m)$ (M_{\odot})	d_{Gaia} (kpc)	L_* (L_{\odot})	$T_{\text{eff}}^{\text{SED}}$ (K)	d_{prim}	RVb ph.	$\Delta t_{\text{obs}}/P_{\text{orb}}$ (%)	Refs.
AI Sco	17530-3348	977 [†]	–	–	2.9 ^{+0.5} _{-0.3}	5600 ⁺¹⁸⁰⁰ ₋₁₄₀₀	4500 ± 250	-2.13	y	3.3	2, 3, 4
EN TrA	14524-6838	1488 ± 9	2.11 ± 0.09	0.57 ± 0.07	2.7 ^{+0.2} _{-0.3}	2800 ⁺²⁵⁰⁰ ₋₄₀₀	5500 ± 250	-2.86	n	1.9	1, 3, 4
HD 95767	11000-6153	1990 ± 60	2.14 ± 0.16	0.33 ± 0.07	4.4 ^{+0.3} _{-0.3}	14 800 ^{+15 500} ₋₂₅₀₀	7100 ± 250	-3.19	y	2.0	1, 3, 4, 7
HD 108015	12222-4652	906 ± 6	0.28 ± 0.02	0.0036 ± 0.0009	5.1 ^{+0.8} _{-0.6}	19 800 ⁺⁵³⁰⁰ ₋₄₄₀₀	6850 ± 250	-3.16	n	5.0	1, 3, 4
HR 4049	10158-2844	430.6 ± 0.1	0.627 ± 0.010	0.177 ± 0.008	1.4 ^{+0.3} _{-0.2}	12 600 ^{+8 200} ₋₂₀₀₀	7200 ± 250	-3.14	y	3.5	1, 2, 3, 4, 5
IRAS 15469-5311	–	390.2 ± 0.7	0.438 ± 0.015	0.074 ± 0.008	3.5 ^{+0.4} _{-0.3}	16 400 ^{+11 900} ₋₁₄₀₀	7000 ± 250	-3.17	n	7.7	1, 3, 4
IW Car	09256-6324	1449 [†]	–	–	1.310 ^{+0.060} _{-0.070}	5500 ⁺⁴⁸⁰⁰ ₋₁₈₀₀	6500 ± 250	-3.17	y	5.6	2, 3, 4
PS Gem	07008+1050	1288.6 ± 0.3	1.507 ± 0.034	0.274 ± 0.019	1.8 ^{+0.1} _{-0.1}	3300 ⁺¹¹⁰⁰ ₋₁₀₀	6100 ± 250	-3.03	y	8.7	1, 3, 4, 6

Notes. The binary period P_{orb} , projected primary semi-major axis $a_1 \sin i_{\text{bin}}$ and mass function $f(m)$ are derived from SB1 fitting by (1). When RV monitoring is unavailable – as marked by [†] – P_{orb} is instead taken to be the period of the detected RVb phenomenon by (2). System distances d_{Gaia} are based on the Gaia DR3 ‘geometric’ estimates by (3). Primary luminosities L_* and effective temperatures $T_{\text{eff}}^{\text{SED}}$ (formal uncertainty of 250 K) are derived from the SED fits by (4). The errors on L_* result from uncertainty on the total reddening. The primary’s H band spectral index d_{prim} (defined at $\lambda_0 = 1.65 \mu\text{m}$), is derived from a power-law fit to the de-reddened model spectrum. We also note detections of the RVb phenomenon, as found by (2), (5), (6) and (7). $\Delta t_{\text{obs}}/P_{\text{orb}}$ denotes the ratio between the timespan within which the observations were taken and the binary period.

References. (1) Oomen et al. (2018); (2) Kiss & Bódi (2017); (3) Bailer-Jones et al. (2021); (4) Kluska et al. (2022); (5) Waelkens et al. (1991a); (6) Van Winckel et al. (1999); (7) Kiss et al. (2007).

target selection is described below. Further details of the data and observations are given in Sect. 3.

The INSPIRING targets were selected out of the wider sample of ~ 85 known Galactic disc-bearing post-AGB binaries (Kluska et al. 2022). This was based on the following selection criteria:

Criterion 1: The target is observable with both PIONIER and GRAVITY – with analysis of the GRAVITY snapshot data being deferred to future work – on the VLTI auxiliary telescopes (ATs), satisfying constraints on correlated flux and sky position.

Criterion 2: An estimated binary orbital period of $P_{\text{orb}} > 1$ yr (Table 1), permitting the necessary AT array configuration changes for imaging with minimal orbital motion during the observing campaign (see Sect. 3).

Criterion 3: Clearly resolved circumstellar emission in prior PIONIER snapshots (Kluska et al. 2019), as shown by a long-baseline plateau in the squared visibilities ($V2$, Sect. 3).

Applying these criteria yielded 11 targets. In this work, we analysed eight of these with clear disc contributions in their PIONIER data and excluded three – IRAS 08544-4431, HR 4226, and U Mon – from our analysis. Briefly, IRAS 08544-4431 is reserved for a dedicated PIONIER time-series imaging; HR 4226 shows no clear H band disc signal in PIONIER (though the outer disc is resolved with the VLT/SPHERE imager by Andrych et al. 2025), and its small radial-velocity amplitudes together with a relatively low effective temperature ($T_{\text{eff}} \approx 4000$ K) cast doubt on its post-AGB classification (Andrych et al. 2025). Hence, we defer a separate, multi-wavelength study; and for U Mon the PIONIER observables seemingly only probe the binary. The inner rim is likely further out and colder, and hence undetectable in NIR, consistent with U Mon’s SED categorisation as a possible transition disc system (Kluska et al. 2022, with the outer disc being resolved with SPHERE by Andrych et al. 2023).

Based on their SEDs, the eight systems analysed in this work are all classified as full discs by Kluska et al. (2022), i.e. with inner rims close to the sublimation radius. This is a selection bias due to the natural tendency of this class of objects to have strong NIR excesses, and thus for the disc signal to be resolvable within PIONIER’s sensitivity limits in the first place. Nevertheless, they form a diverse sample of post-AGB binaries, covering a broad range in orbital period, stellar effective temperature and lumi-

nosity, refractory depletion level and previous inclination angle estimates. The main target properties relevant to our analysis and interpretation are summarised in Table 1. For completeness, we give extensive descriptions of pertinent results from previous literature on these targets in Appendix A.

3. Data and observations

For our eight targets (Sect. 2), we obtained VLTI/PIONIER (Le Bouquin et al. 2011) observations in the H band using the ATs in various configurations. A grism disperses the light into six spectral channels ($R \sim 30$; $1.50 - 1.80 \mu\text{m}$). Each PIONIER integration delivers six baseline squared visibility ($V2$) and four (of which three are independent) triplet closure phase ($\phi3$) measurements for every spectral channel. While the former is sensitive to the radial intensity dependence of the source along different directions, the latter constrains its point-asymmetry. Each target was assigned six K-type giant calibrators at on-sky separations of $< 5^\circ$ found using SearchCal¹ (Chelli et al. 2016), excluding objects with uncertain luminosity class, known variability, or multiplicity. Every two science observations were bracketed – in a CAL-SCI-CAL-SCI-CAL sequence – by observations of three different calibrators.

To enable imaging, the observations were taken using various AT configurations (baselines spanning $\sim 10 - 130$ m) to properly fill the spatial frequency plane (also called the (u, v) plane). We retrieved all reduced and calibrated INSPIRING observations from the Jean-Marie Mariotti Center Optical Interferometry Database (OiDB)². The data were reduced using the standard pndrs³ data reduction package (Le Bouquin et al. 2011). We then filtered the observations based on any severe problems with fringe tracking, weather conditions, etc. Observations showing a less than optimal ESO quality control grade (i.e. grade B or C) were manually checked. Any such observations that still presented good quality data on > 4 baseline pairs were kept. Some observations were graded poor due to (u, v) plane overlap with previous observations, while still showing excellent data quality.

¹ <https://www.jmmc.fr/searchcal>

² <http://oidb.jmmc.fr>

³ <http://www.jmmc.fr/pionier>

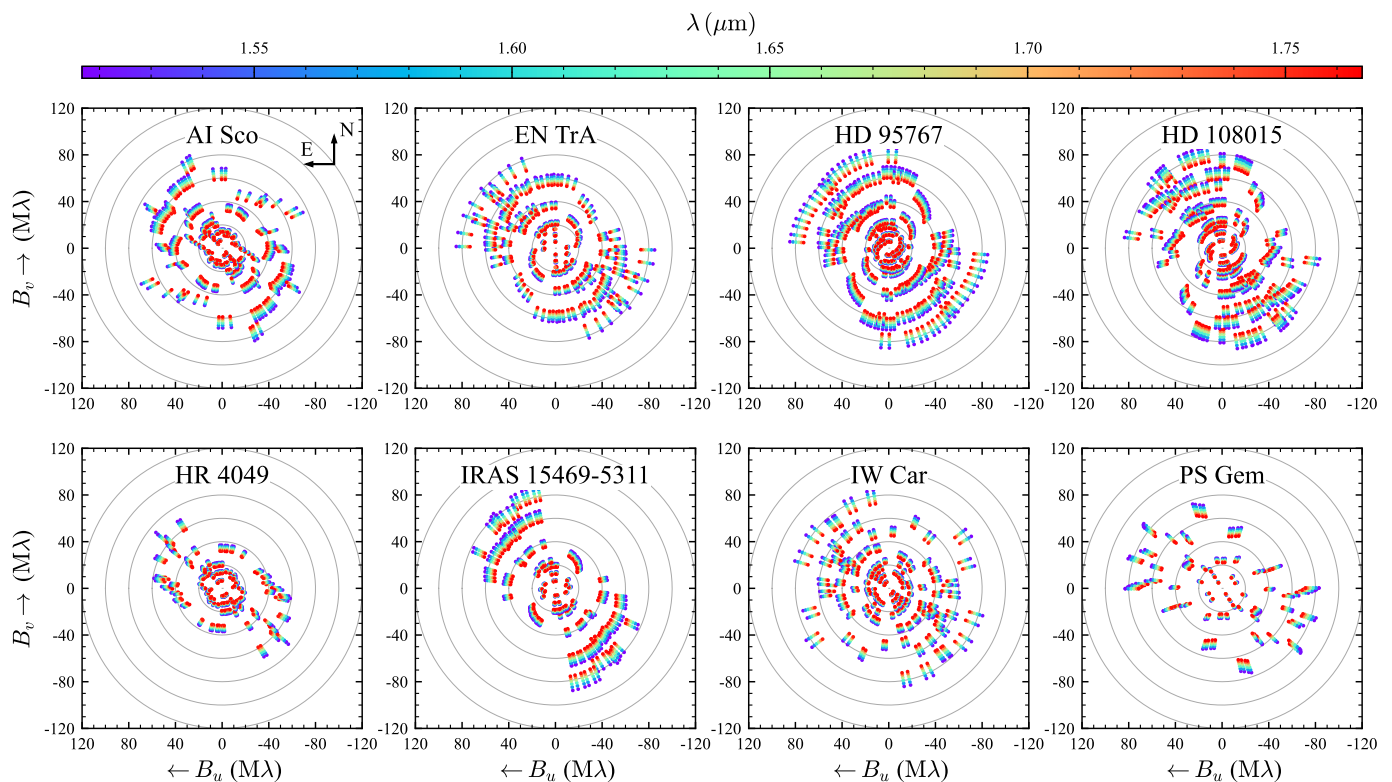


Fig. 1: (u, v) coverage for the targets' selected data. Observations are denoted by scattered circles, coloured by their wavelength.

To minimise the effects of orbital motion and variable illumination on the inner disc, we carefully selected observations within the smallest possible time window that still provided adequate (u, v) coverage for imaging. This strategy avoids merging widely separated epochs, which could otherwise introduce time-dependent signatures. The fractional time-span of the selected observations relative to the orbital period, $\Delta t_{\text{obs}}/P_{\text{orb}}$, is typically only a few per cent (Table 1), ensuring that orbital smearing has a limited impact on the reconstructed morphologies.

Logs of the selected observations including the observational conditions and calibrators are available online on [Zenodo](#). The (u, v) coverages, dirty beams (i.e. the point spread functions, the centre of which forms the formal resolution element called the 'beam size') and corresponding V_2 and ϕ_3 data are shown in Figs. 1, F.1 & E.1, respectively.

4. Methodology

Given that the inner disc regions are expected to be morphologically complex, the principal aim of the analysis is to produce non-parametric image reconstructions of the circumstellar environment. Our imaging workflow makes use of the SPARCO formalism, which we describe in Sect. 4.1. To provide initial estimates on the different SPARCO parameters (flux ratios, chromaticities and positions), we perform a simplified geometric modelling of our targets in Sect. 4.2. Lastly, our image reconstruction workflow itself is described in Sect. 4.3.

4.1. The SPARCO visibility formalism

In the H band, the primary star presents itself as a bright central emission, while the disc emission is much more diffuse. In addition, the data show strong chromaticity, caused by the relative

flux change between the primary and disc (revealed by the strong V_2 slopes across wavelength channels in Fig. E.1). We addressed these challenges by adopting the Semi-Parametric Approach for Reconstruction of Chromatic Objects (SPARCO, [Kluska et al. 2014](#)). SPARCO defines the total source visibility $\tilde{V}(u, v)$ as a flux-weighted combination of the central stars and the circumstellar environment:

$$\tilde{V}_{\text{tot}}(u, v, \lambda) = \frac{\sum_j f_j(\lambda) \tilde{V}_j(u, v)}{\sum_j f_j(\lambda)}, \quad (1)$$

$$f_j(\lambda) = f_{j,0} (\lambda/\lambda_0)^{d_j}, \quad (2)$$

$$\sum_j f_{j,0} = 1, \quad (3)$$

where j represents a component – in our case the primary star, secondary star or disc rim – and f_j its spectrum. Following [Kluska et al. 2019](#), we defined the spectrum by a spectral index d_j and flux fraction $f_{j,0}$ at reference wavelength $\lambda_0 = 1.65 \mu\text{m}$. This assumes constant component morphologies across wavelength channels, which is reasonable for the narrow H band. The essence of SPARCO is then to approximate the central stars in Eq. 1 using closed-form geometric components, while applying an image reconstruction algorithm to recover just the disc rim $\tilde{V}_{\text{rim}}(u, v)$. This greatly reduces the required pixel dynamic range and allows us to use data from all wavelength channels simultaneously, significantly improving image fidelity and the capability to spatially separate the central stars from the disc rim.

Throughout the remainder of this work, we refer to the central star geometric parameters as the 'SPARCO parameters'. We modelled the primary as a uniform disc centred at the origin and the secondary as a point source. The SPARCO parameters are then the primary's flux fraction $f_{\text{prim},0}$, uniform diameter UD_{prim}

and spectral index d_{prim} , the disc spectral index d_{rim} , and the secondary's flux fraction $f_{\text{sec},0}$ and position $(\Delta\alpha_{\text{sec}}, \Delta\delta_{\text{sec}})$. Throughout our analysis, we fixed d_{prim} to the value derived from the SED fit (Table 1). This is because our data are only sensitive to relative flux differences between components. The SPARCO parameter values need fine-tuning in order to properly reveal the circumstellar environment (cf. Kluska et al. 2014, 2016, 2020a).

We combined SPARCO with an image reconstruction algorithm and a SPARCO parameter optimisation routine into a consistent image reconstruction workflow, which we describe in Sect. 4.3. To proceed with image reconstruction, however, we first required preliminary estimates on the SPARCO parameters, which we obtained via a simplified geometric modelling of the binary and inner rim.

4.2. Initial SPARCO estimates via geometric modelling

To provide a first estimate of the SPARCO parameters, we fitted simple geometric models to the data using PMOIRE⁴ (Mérand 2022). PMOIRE allows the user to flexibly define the source morphology as a combination of parametrised components. We adopted the visibility model of Eq. 1. This step of the analysis is designed to provide initial estimates of the SPARCO parameters (Sect. 4.1), as these provide crucial input for our imaging workflow.

PMOIRE fits parameters by minimising the reduced χ^2_{ν} using a Levenberg-Marquardt algorithm (Marquardt 1963). To avoid local minima, we opted to gradually increase our model complexity, using the best fit from the previous model as a starting point for the next (similar to the strategy adopted by Kluska et al. 2019). We proceeded through the following stages:

Step 1: primary and symmetric power law disc. Assuming a maximum primary stellar diameter of $300 R_{\odot}$ (e.g. Bollen et al. 2022), we fitted it using a uniform disc of diameter UD_{prim} , on the condition that the corresponding angular size of the maximum stellar diameter is above half of the interferometric beam size. If lower, we modelled the primary as a point source. The inner disc rim was modelled as an azimuthally symmetric disc with a radial power law surface brightness. It is inclined with inclination i_{rim} and oriented by position angle PA_{rim} , defined anti-clockwise from north to east. We note that the derived inclination assumes a circular rim, where the only source of ellipticity is its on-sky projection. The rim is further defined by its flux fraction $f_{\text{disc},0}$, inner diameter θ_{rim} (interior to which the intensity is zero), outer diameter θ_{out} , radial brightness power index ρ_{rim} and spectral index d_{rim} . θ_{out} is fixed to an angular size corresponding to 300 AU. Our data only probe the inner disc, so its value has little effect on the results. Both components were centred at $(0, 0)$.

In addition, we added a grey over-resolved background of flux $f_{\text{bkg},0}$, on the condition that it improves the short baseline $V2$ residuals and causes a decrease of the Bayesian information criterion (BIC, Schwarz 1978) $\Delta\text{BIC} < -100$. We adopted this conservative BIC threshold (a more common choice is $\Delta\text{BIC} < -10$) because the errors on PIONIER data can be underestimated (as is generally the case for interferometric instruments, e.g. Monnier et al. 2012; GRAVITY Collaboration et al. 2019), and more lenient thresholds often resulted in overfitting.

Step 2: primary with offset and azimuthally modulated disc. The disc centre was offset from the primary by $(\Delta\alpha_{\text{rim}}, \Delta\delta_{\text{rim}})$. In another fit, the disc brightness was azimuthally modulated using a first order harmonic, as described by its amplitude $A_{\text{mod},1}$ and

position angle relative to the PA of the rim $\psi_{\text{mod},1}$. Each complexity increase was again only accepted if $\Delta\text{BIC} < -100$.

Step 3: binary with offset and azimuthally modulated disc. A grey point-source secondary companion was added to the fit (chromatic companions did not improve the BIC). It is defined by its flux fraction $f_{\text{sec},0}$ and offset from the primary $(\Delta\alpha_{\text{sec}}, \Delta\delta_{\text{sec}})$ (initially set to the disc centre found in step 2). We stress that the secondary's flux is likely not photospheric, instead originating from jet-launching circumcompanion accretion discs (e.g. Hillen et al. 2016; Bollen et al. 2022; Verhamme et al. 2024; De Prins et al. 2024). We added this component only if $\Delta\text{BIC} < -100$.

Step 4: correction of the secondary detection via preliminary reconstructions. Due to our simplistic model of the inner rim (including only a first order azimuthal modulation), step 3 can be highly degenerate and prone to placing a secondary at unphysical positions, mimicking rim morphology features. As a result, we included a feedback step from the image reconstructions in order to validate the secondary detections, and, if necessary, repeated step 3 with a corrected initial secondary position. We provide a further description of this feedback step in Sect. 4.3.4.

Parameter uncertainties on the final geometric models were obtained via bootstrapping (Efron 1979), using 20 000 samples. The only target to which we could not fit a geometric model is IW Car, as its complex morphology proved unable to be reproduced with a single-disc model (see also Fig. 4). We tested two-disc models for IW Car, but these resulted in ill-conditioned solutions with large parameter degeneracies, providing no meaningful constraints as the PMOIRE minimisation engine became immediately trapped in local minima. We therefore restricted our analysis to single-disc models for compatibility across the sample. The parameters of our final geometric model fits are found in Table 2. The corresponding model disc images are presented in Fig. B.1, though we note that the images are not used as initial starting points for the image reconstructions.

4.3. Image reconstruction workflow

Image reconstruction allows us to represent the source morphology in a non-parametric way, providing a powerful tool for discovering unexpected features whose presence could be difficult to decidedly infer using parametric models. However, sparse (u, v) coverages and non-linearity between source morphology and observables make it an ill-posed, non-convex inverse problem (Thiébaud & Young 2017). As a result, the loss function to be minimised is typically formulated in a Bayesian way:

$$\mathcal{L}_{\text{tot}} = \mathcal{L}_{\text{data}} + \mu\mathcal{L}_{\text{reg}}, \quad (4)$$

consisting of both a data loss $\mathcal{L}_{\text{data}}$ and a prior-like regularisation function \mathcal{L}_{reg} . Many different images can fit the data well, leading to low $\mathcal{L}_{\text{data}}$ despite not being astrophysically valid. The role of \mathcal{L}_{reg} is to reign in the reconstruction, guiding it toward images with certain qualitative properties. Its relative numerical weight in the reconstruction is set via the regularisation weight μ .

4.3.1. ORGANIC image reconstruction

For our image reconstructions, we utilised the ORGANIC⁵ algorithm (Claes et al. 2020). It uses a Generative Adversarial Network (GAN, Goodfellow et al. 2014) – a type of convolutional neural network (CNN) – to encode RT models as physically informed priors for image reconstruction. Specifically, ORGANIC

⁴ <https://github.com/amerand/PMOIRE>

⁵ <https://github.com/DePrinsT/organic>

Table 2: Best fit parameters of the final geometric models.

Target	χ^2_{ν}	$f_{\text{prim},0}$ (%)	UD _{prim} (mas)	$f_{\text{bg},0}$ (%)	$f_{\text{sec},0}$ (%)	$\Delta\alpha_{\text{sec}}$ (mas)	$\Delta\delta_{\text{sec}}$ (mas)	θ_{rim} (mas)	i_{rim} ($^\circ$)	PA _{rim} ($^\circ$)	$\Delta\alpha_{\text{rim}}$ (mas)	$\Delta\delta_{\text{rim}}$ (mas)	ρ_{rim}	d_{rim}	$A_{\text{mod},1}$	$\psi_{\text{mod},1}$ ($^\circ$)	r_{hl}^a (mas)
AI Sco	4.98	68.1 $^{+0.4}_{-0.4}$	–	–	5.9 $^{+0.2}_{-0.2}$	-1.08 $^{+0.04}_{-0.03}$	-1.38 $^{+0.06}_{-0.06}$	5.83 $^{+0.09}_{-0.07}$	45.6 $^{+2.0}_{-1.6}$	60 $^{+7}_{-5}$	-0.53 $^{+0.07}_{-0.11}$	-1.86 $^{+0.12}_{-0.09}$	-6.7 $^{+0.7}_{-0.9}$	0.2 $^{+0.2}_{-0.2}$	0.87 $^{+0.05}_{-0.05}$	-9 $^{+4}_{-5}$	3.41 $^{+0.09}_{-0.08}$
EN TrA	2.40	72.1 $^{+0.4}_{-0.4}$	–	–	5.0 $^{+0.2}_{-0.2}$	-0.70 $^{+0.02}_{-0.02}$	-1.65 $^{+0.04}_{-0.04}$	5.63 $^{+0.16}_{-0.14}$	58.9 $^{+1.1}_{-1.2}$	32.5 $^{+1.9}_{-1.7}$	-1.13 $^{+0.07}_{-0.07}$	-1.15 $^{+0.10}_{-0.12}$	-3.97 $^{+0.10}_{-0.10}$	4.37 $^{+0.11}_{-0.11}$	0.72 $^{+0.04}_{-0.04}$	-13 $^{+4}_{-4}$	4.02 $^{+0.08}_{-0.08}$
HD 95767	1.97	48.5 $^{+0.7}_{-0.7}$	–	–	21.0 $^{+0.7}_{-0.7}$	-0.719 $^{+0.013}_{-0.013}$	-0.510 $^{+0.009}_{-0.009}$	4.67 $^{+0.05}_{-0.04}$	25.6 $^{+1.7}_{-1.7}$	14 $^{+4}_{-4}$	0.11 $^{+0.04}_{-0.03}$	-0.61 $^{+0.04}_{-0.03}$	-3.83 $^{+0.03}_{-0.03}$	6.39 $^{+0.08}_{-0.08}$	0.451 $^{+0.019}_{-0.020}$	43 $^{+4}_{-4}$	3.41 $^{+0.03}_{-0.03}$
HD 108015	2.08	61.8 $^{+0.3}_{-0.3}$	–	8.6 $^{+0.5}_{-0.4}$	–	–	–	5.63 $^{+0.03}_{-0.03}$	31.2 $^{+0.7}_{-0.8}$	82.5 $^{+1.2}_{-1.1}$	-0.612 $^{+0.018}_{-0.017}$	0.53 $^{+0.02}_{-0.02}$	-5.64 $^{+0.10}_{-0.12}$	7.09 $^{+0.09}_{-0.08}$	0.502 $^{+0.008}_{-0.007}$	-66 $^{+2}_{-2}$	3.419 $^{+0.014}_{-0.014}$
HR 4049 ^b	1.71	65.92 $^{+0.14}_{-0.14}$	0.74 $^{+0.02}_{-0.02}$	–	0.42 $^{+0.05}_{-0.05}$	-1.70 $^{+0.07}_{-0.08}$	-0.69 $^{+0.10}_{-0.09}$	14.33 $^{+0.16}_{-0.18}$	56.8 $^{+1.0}_{-1.0}$	82.32 $^{+1.0}_{-0.8}$	-1.70 $^{+0.07}_{-0.08}$	-0.69 $^{+0.10}_{-0.09}$	-2.73 $^{+0.04}_{-0.05}$	7.90 $^{+0.07}_{-0.07}$	0.42 $^{+0.03}_{-0.03}$	-38 $^{+3}_{-3}$	15.44 $^{+0.46}_{-0.46}$
IRAS 15469-5311	2.08	59.5 $^{+0.7}_{-0.6}$	–	11.1 $^{+1.2}_{-1.1}$	–	–	–	7.80 $^{+0.05}_{-0.06}$	40.2 $^{+0.8}_{-0.7}$	53.5 $^{+1.0}_{-1.1}$	0.31 $^{+0.03}_{-0.03}$	-0.39 $^{+0.02}_{-0.02}$	-4.84 $^{+0.13}_{-0.14}$	8.51 $^{+0.21}_{-0.19}$	0.86 $^{+0.02}_{-0.02}$	74.6 $^{+1.6}_{-1.5}$	5.00 $^{+0.05}_{-0.05}$
PS Gem ^b	0.94	89.01 $^{+0.14}_{-0.14}$	0.44 $^{+0.02}_{-0.02}$	–	–	–	–	8.4 $^{+0.6}_{-0.6}$	39 $^{+6}_{-7}$	156 $^{+5}_{-6}$	–	–	-2.79 $^{+0.22}_{-0.17}$	4.3 $^{+0.2}_{-0.2}$	0.65 $^{+0.06}_{-0.05}$	35 $^{+9}_{-11}$	9.1 $^{+1.3}_{-0.8}$

Notes. ^(a) Different parametrisations can have different biases in the rim diameter. To facilitate comparison with other geometric and RT models (e.g. [Corporaal et al. 2023b](#)), we also calculated the disc half-light radius, r_{hl} , using elliptical apertures following the inner rim orientation. It is a more robust tracer of the overall rim emission size (cf. [Varga et al. 2021](#)). ^(b) For HR 4049 and possibly PS Gem, r_{hl} is strongly overestimated, likely because the rim model tries partially account for an over-resolved flux component (causing their high ρ_{rim} values). Their r_{hl} and ρ_{rim} values should be treated with caution.

is trained on an extensive grid of H and K band thermal dust emission models of symmetric disc rims, simulated using the MCMMax⁶ RT code ([Min et al. 2009](#)). We briefly describe the ORGANIC algorithm below, but refer interested readers to [Claes et al. \(2020\)](#) for more details.

The GAN architecture consists of a ‘generator’ and a ‘discriminator’. The generator takes a size 100 latent Gaussian noise vector and maps it to a 128×128 image. The discriminator takes a 128×128 image and maps it to a scalar score $\hat{s} \in [0, 1]$. The overall ORGANIC algorithm consists of the following two steps:

Step 1: initial training. The generator and discriminator are iteratively and alternately trained. In each training step, the generator produces a batch of ‘fake’ images using a set of random input noise vectors. These are presented to the discriminator together with a batch of ‘real’ images from the RT training set. In alternating fashion, the generator is trained to deceive the discriminator into evaluating its images as real (aiming at a discriminator score $\hat{s} \sim 1$ for its images), while the discriminator is trained to discern the ‘fake’ generator images from the ‘real’ RT ones (aiming for $\hat{s} \sim 0$ and $\hat{s} \sim 1$ for the generated and RT images, respectively). When properly trained, this adversarial game converges to a state where the generator produces an image distribution similar to the RT models ([Goodfellow et al. 2014](#)).

Step 2: image reconstruction. The GAN can then be confronted with any set of V2 and $\phi 3$ data. With the discriminator fixed, the generator starts from a random latent noise vector. This essentially corresponds to drawing a random initial image similar to the RT training images. The generator is then further trained to minimise Eq. 4 by directly updating the weights in its convolutional kernels. The loss terms are now:

$$\mathcal{L}_{\text{data}} = \frac{l_{V2} + l_{\phi 3}}{N_{V2} + N_{\phi 3}}, \quad (5)$$

$$l_{V2} = \sum_{i=1}^{N_{V2}} \frac{(V2_{\text{obs},i} - V2_{\text{img},i})^2}{\sigma_{V2,i}^2} = \chi^2_{V2}, \quad (6)$$

$$l_{\phi 3} = \sum_{i=1}^{N_{\phi 3}} \frac{2(1 - \cos(\phi 3_{\text{obs},i} - \phi 3_{\text{img},i}))}{\sigma_{\phi 3,i}^2}, \quad (7)$$

$$\mathcal{L}_{\text{reg}} = -\ln \hat{s}_{\text{img}}, \quad (8)$$

with the subscripts ‘img’ and ‘obs’ respectively denoting the generated image and the observed data. N_{V2} and $N_{\phi 3}$ are the number of observed V2 and $\phi 3$ points, and l_{V2} and $l_{\phi 3}$ the corresponding data losses. We assumed a Von Mises distribution for $\phi 3$ in order to account for its angular nature. The goal of \mathcal{L}_{reg} is to make the final images look more like the RT training models. However, most of the regulatory properties of ORGANIC are implicitly inherited from the CNN architecture and the initial training. We demonstrate and discuss this in Appendix C.

To account for the random nature of the starting vector, ORGANIC repeats this step for N_{restart} different random generator inputs. We set $N_{\text{restart}} = 50$. This results in an image cube, the median of which is adopted as the final image. The standard deviation along the cube for each pixel j , $\sigma_{\text{restart},j}$, then represents the uncertainty induced by the choice of latent vector. Regardless, some of the N_{restart} images in the cube are badly converged, ending up in poor local minima. To account for this, we added a procedure using principal component analysis (e.g. [Gewers et al. 2021](#)) and k-means clustering ([Lloyd 1982](#)) to filter out these images from the cube. We applied PCA to the image cube, retaining 15 components to reduce dimensionality (accounting

⁶ <https://github.com/michielmin/MCMMax3D>

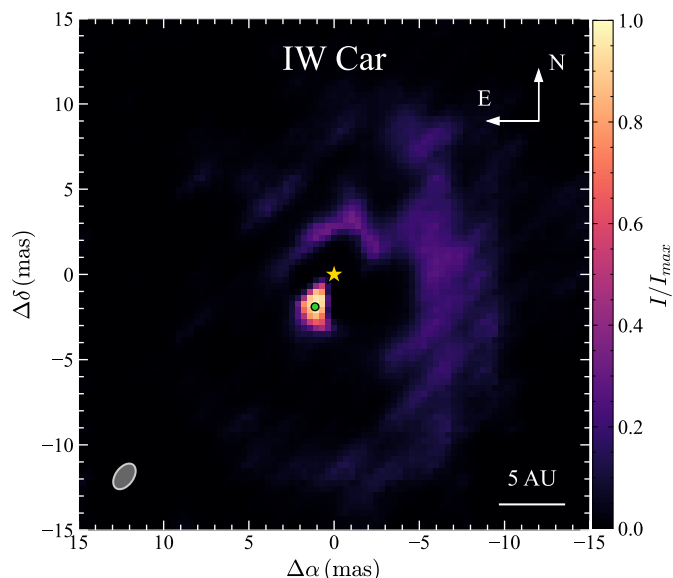


Fig. 2: Peak-normalised IW Car ORGANIC image without a SPARCO secondary. We identify a strong unresolved flux peak as flux from the secondary. The primary is marked by a gold star, while a green dot marks the centre of an elliptical Gaussian fit to the peak. The interferometric beam size and a 5 AU scale bar are shown in the bottom.

for $\sim 70 - 80\%$ of the inter-image variance). We then applied k-means clustering with three clusters on the PCA subspace, discarding the cluster with the worst median \mathcal{L}_{tot} . This proved highly effective in singling out poorly converged images.

4.3.2. SPARCO optimisation

We applied ORGANIC in combination with the SPARCO approach. Our binaries can have up to six free SPARCO parameters: $f_{\text{prim},0}$, UD_{prim} , d_{rim} , $f_{\text{sec},0}$, $\Delta\alpha_{\text{sec}}$ and $\Delta\delta_{\text{sec}}$ (Sect. 4.1). This made the computational cost of grid searches (e.g. Kluska et al. 2016, 2020a) prohibitive. We instead made use of the BADS⁷ optimisation algorithm (Acerbi & Ma 2017), running ORGANIC for each considered set of SPARCO parameters and choosing the one with the lowest value of \mathcal{L}_{tot} (Eq. 4) on the resulting image. BADS alternates between a broader systematic grid search stage and a fast, detailed local search using a Gaussian process surrogate for \mathcal{L}_{tot} (e.g. Rasmussen & Williams 2006). It is highly efficient in the required amount of ORGANIC runs and can readily escape shallow local minima.

We took the initial SPARCO parameter values from the corresponding final geometric models in Table 2 (after validation and correction of the secondary position from preliminary imaging; see Sect. 4.3.4). Initial tests showed that BADS+ORGANIC had the tendency to place the secondary at non-physical positions and heavily reduce its flux contribution, instead placing a slightly smeared flux in the image reconstruction at the true secondary position. This is likely because the binary motion causes the secondary to better fit the data as a slightly smeared Gaussian instead of a point source. As a result, we fixed $(\Delta\alpha_{\text{sec}}, \Delta\delta_{\text{sec}})$ to their final geometric model values (Table 2), leaving only $f_{\text{prim},0}$, UD_{prim} , d_{rim} and $f_{\text{sec},0}$ free.

⁷ Its Python interface, pyBADs (Singh & Acerbi 2024), is available at <https://github.com/acerbilab/pybads>

Since we could not fit a geometric model for IW Car, the secondary position was instead fully inferred from a Gaussian fit to the strong unresolved flux peak in a BADS+ORGANIC run omitting the secondary star SPARCO component, which is identified as emission from the secondary (cf. Hillen et al. 2016). This resulted in $(\Delta\alpha_{\text{sec}}, \Delta\delta_{\text{sec}}) = (1.12, -1.90)$ mas (Fig. 2). The other initial values were set to the fit values of Kluska et al. (2019), derived from PIONIER snapshot data.

4.3.3. Selection of the regularisation weight and pixel scale

As optimisation of μ via the usual L-curve method (e.g. Renard et al. 2011) is prohibited due to the current ORGANIC architecture (see the discussion in Appendix C), we performed manual exploration in a reasonable range ($\mu = 0.1 - 2$). Finding the same main recovered features for different values (see also Fig. C.1), we fixed $\mu = 0.2$ during our imaging workflow for all targets. This value generally provided a good balance between suppression of reconstruction artefacts while avoiding excessive over-regularisation, which can tend to make the rims too sharp.

Starting from images with a pixel scale corresponding to Nyquist sampling (two pixels fitting in the beam size) we gradually increased the sampling factor. We applied the BADS optimisation each time, until all discs were deemed properly resolved with $\sim 20 - 30$ pixels across the inner rim diameter. During this, we took care to ensure the 128×128 pixel field-of-view (set by the architecture of ORGANIC) contained all of the rim's flux.

4.3.4. Correction of the secondary detection

Due to the simplistic geometric model used for the disc rim, step 3 in the geometric modelling (Sect. 4.2) can initially fit faulty secondary positions. As a result, we first validated the secondary detection by performing preliminary BADS+ORGANIC runs where the secondary was omitted from the SPARCO parameters (i.e. $f_{\text{sec}} = 0$). In the resulting image reconstructions, the secondary emission, if significant, appears as a clear unresolved flux contribution (as seen in Fig. 2 for IW Car). If the model secondary position proved to be mimicking features of the disc rim, we reran the geometric fitting step 3 with a corrected initial position to procure the final geometric models. For HD 108015 the geometric companion detection was fully spurious, and the final geometric model was instead taken from step 2.

4.3.5. Uncertainty estimation

After optimising the SPARCO parameters using BADS, we performed a final bootstrap procedure with 500 resampled datasets, applying ORGANIC to each and storing the resulting final median image in a cube. The standard deviation along this cube was then adopted as the uncertainty induced by the data, $\sigma_{\text{boot},j}$. This was added in quadrature to the restart-induced error, $\sigma_{\text{restart},j}$, of the image reconstructed on the original dataset to provide the total error for each pixel j , i.e. $\sigma_{\text{tot},j} = \sqrt{\sigma_{\text{restart},j}^2 + \sigma_{\text{boot},j}^2}$. This total error was used to calculate any significance contours.

4.3.6. Workflow and image feature validation

We have implemented an extensive suite of tests to validate our imaging workflow and assess the robustness of features detected in the final images.

In Appendix B, we applied our full imaging workflow on synthetic datasets, derived from the PMOIRE model images, to

Table 3: ORGANIC image reconstruction parameters and image-derived inner rim parameters.

Target	SF ^a	PS ^a (mas)	FOV ^a (mas)	$\mathcal{L}_{\text{data}}$	\mathcal{L}_{reg}	$f_{\text{prim},0}$ (%)	UD _{prim} (mas)	$f_{\text{sec},0}$ (%)	d_{rim}	θ_{rim} (mas)	i_{rim} (°)	PA _{rim} (°)	$\Delta\alpha_{\text{rim}}$ (mas)	$\Delta\delta_{\text{rim}}$ (mas)	r_{hl} (mas)
AI Sco ^b	5	0.230	29.5	2.09	0.94	64.5	–	2.76	–0.59	$4.8^{+0.8}_{-0.5}$	46^{+10}_{-14}	135^{+7}_{-7}	$0.51^{+0.13}_{-0.15}$	$-1.4^{+0.3}_{-0.2}$	$2.89^{+0.12}_{-0.23}$
EN TrA	4	0.265	33.9	1.63	0.91	72.1	–	5.37	0.30	$6.1^{+0.3}_{-0.2}$	50^{+3}_{-4}	37^{+5}_{-7}	$-1.02^{+0.09}_{-0.09}$	$-0.89^{+0.17}_{-0.21}$	$3.99^{+0.13}_{-0.27}$
HD 95767	4	0.263	33.7	0.96	0.97	44.1	–	24.75	2.36	$6.01^{+0.05}_{-0.05}$	$23.7^{+1.0}_{-0.5}$	7^{+8}_{-5}	$0.03^{+0.03}_{-0.03}$	$-0.51^{+0.03}_{-0.03}$	$3.43^{+0.13}_{-0.13}$
HD 108015	3	0.327	41.9	0.99	0.93	56.0	–	–	1.45	$6.28^{+0.06}_{-0.06}$	30^{+3}_{-3}	81^{+5}_{-5}	$-0.57^{+0.04}_{-0.04}$	$0.58^{+0.06}_{-0.06}$	$3.78^{+0.16}_{-0.16}$
HR 4049 ^b	2	0.635	81.3	0.97	0.92	65.4	0.72	0.24	2.39	$17.2^{+1.5}_{-1.2}$	48^{+4}_{-4}	95^{+8}_{-8}	$-1.5^{+0.6}_{-0.8}$	$-0.4^{+0.3}_{-0.3}$	$16.5^{+3.6}_{-1.9}$
IRAS 15469-5311	3	0.294	37.6	0.82	0.89	52.9	–	–	1.84	$8.99^{+0.09}_{-0.09}$	35^{+2}_{-2}	51^{+3}_{-3}	$0.23^{+0.06}_{-0.06}$	$-0.29^{+0.05}_{-0.05}$	$5.3^{+0.3}_{-0.2}$
IW Car ^c	3	0.350	44.8	1.52	0.95	63.6	0.50	1.99	0.89	$6.9^{+0.5}_{-0.5}$	48^{+5}_{-5}	144^{+8}_{-7}	$0.15^{+0.19}_{-0.18}$	$-0.1^{+0.2}_{-0.2}$	$11.7^{+1.0}_{-0.4}$
										$20.3^{+0.9}_{-0.8}$	57^{+2}_{-2}	176^{+3}_{-3}	$-1.0^{+0.3}_{-0.2}$	$-1.4^{+0.4}_{-0.4}$	$11.9^{+1.0}_{-0.3}$
PS Gem ^b	3	0.311	39.8	0.71	0.88	87.0	0.37	–	0.61	$9.0^{+0.4}_{-0.3}$	28^{+5}_{-3}	161^{+7}_{-12}	$0.027^{+0.15}_{-0.15}$	$-0.4^{+0.2}_{-0.2}$	$7.5^{+0.8}_{-0.8}$

Notes. The secondary positions ($\Delta\alpha_{\text{sec}}, \Delta\delta_{\text{sec}}$) are the same as in Table 2 (except IW Car, where ($\Delta\alpha_{\text{sec}}, \Delta\delta_{\text{sec}}$) = (1.12, –1.90) mas following Fig. 2). ^(a) SF, PS & FOV are the image sampling factor (i.e. how many pixels fit in the beam size), pixel scale and field-of-view. ^(b) HR 4049 and possibly PS Gem likely have overestimated r_{hl} values, since their images account for an over-resolved flux component (see Fig. 7). Similarly, r_{hl} could be slightly underestimated for AI Sco, since the flux close to the primary is systematically offset southwards (see Sect. 5.3.1). ^(c) For IW Car, we find both inner flux arcs and a large outer flux arc (see Sect. 5.3.7), and we provide fits for both.

identify potential biases in the inner rim parameters and the general position of azimuthal brightness enhancements. Appendix D presents image reconstructions performed with the more classical SQUEEZE reconstruction package (Baron et al. 2010). The physics-informed regularisation capabilities of ORGANIC (Sect. 7) allowed us to reconstruct coherent images for HR 4049 and PS Gem, where SQUEEZE failed as it heavily overfitted the data due to the sparser (u, v) coverage. Otherwise, SQUEEZE recovers the same general features as our ORGANIC images, confirming the convergence of our ORGANIC workflow. Lastly, Appendix F assesses the robustness of the image features against the specifics of the (u, v) coverage and dirty beam artefacts. In what follows, we will address the robustness of image features revealed by our tests when needed.

5. Results

We applied the image reconstruction workflow developed in Sect. 4 to our eight targets (Sect. 2), providing high fidelity, non-parametric images of their circumstellar environment. The parameters for our final ORGANIC images are summarised in Table 3, while the reconstructed images themselves are shown in Figs. 3 & 4. The dusty inner disc rim is well-resolved for all targets. We first present a fitting routine to extract the overall inner rim properties and radial surface brightness profiles in Sect. 5.1, and briefly describe the derived rim inclinations in the context of the ‘RVb phenomenon’ (long-term secular brightness modulations following P_{orb} ; see e.g. Manick et al. 2017) in Sect. 5.2. We then describe the detected morphological features in Sect. 5.3. A comprehensive discussion of the possible underlying physical mechanisms is presented in Sect. 6.

5.1. Rim fitting and brightness profile calculation

We developed an ellipse fitting procedure to retrieve the inner rim parameters directly from the images. Radial rays were drawn from the primary every 10° azimuthally, including only rim sections of higher per-pixel significance ($\geq 3\sigma$ for all targets except PS Gem, for which we use $\geq 2\sigma$). A Gaussian was matched

to each ray’s radial profile to constrain the radial position of peak brightness. This was repeated for every image in the ORGANIC cubes to determine the rim positions and their uncertainties, taken as the median and standard deviation across the cube. For AI Sco, we placed a 0.9 mas diameter circular mask over the primary during this procedure, since the image flux close to its position is likely biased slightly southwards (see Sect. 5.3.1).

An ellipse was then fit to the positions in order to derive the rim parameters and their uncertainties. For this, we used the Markov Chain Monte Carlo (MCMC) package emcee⁸ (Foreman-Mackey et al. 2013) with 32 walkers performing 100 000 steps each. An example of this procedure is shown in Fig. 5. The resulting inner rims are displayed on Figs. 3 & 4, and their parameters summarised in Table 3. We stress that the emission does not probe the mid-plane, but originates from (sub-) μm grains lifted to layers around 1–2 gas scale heights higher up (e.g. Hillen et al. 2014; Kluska et al. 2018). On-sky projection can then skew the centre of emission ($\Delta\alpha_{\text{rim}}, \Delta\delta_{\text{rim}}$) along the projected rim’s minor axis, away from the centre of mass (e.g. de Boer et al. 2016). We note that in case the inner rim is sharp and wall-like, the limited beam size of the observations causes the imaged morphology of the rim to be slightly washed out. This can cause our rim fitting method to induce a systematic positive bias of typically $\lesssim 1$ mas ($\lesssim 2$ mas for HR 4049 & PS Gem) in θ_{in} and a negative bias of $\lesssim 10^\circ$ in i_{rim} relative to the true values (see Sect. B.1). However, at least for rims set by sublimation physics, there is little reason to suspect the rim would be sharp in the first place (see Sect. 6.1.1).

Using concentric elliptical apertures following the rim orientations (Table 3), we then calculated radial surface brightness profiles. This was again repeated for every image in the image cubes to provide 1σ uncertainties. The resulting profiles are shown in Fig. 7. For IW Car, where we find both inner flux arcs and a large outer flux arc (see Sect. 5.3.7), the rim fitting procedure was applied to both features. The IW Car brightness profile calculation was based on the orientation of the rim fit to the inner arcs.

⁸ <https://github.com/dfm/emcee>

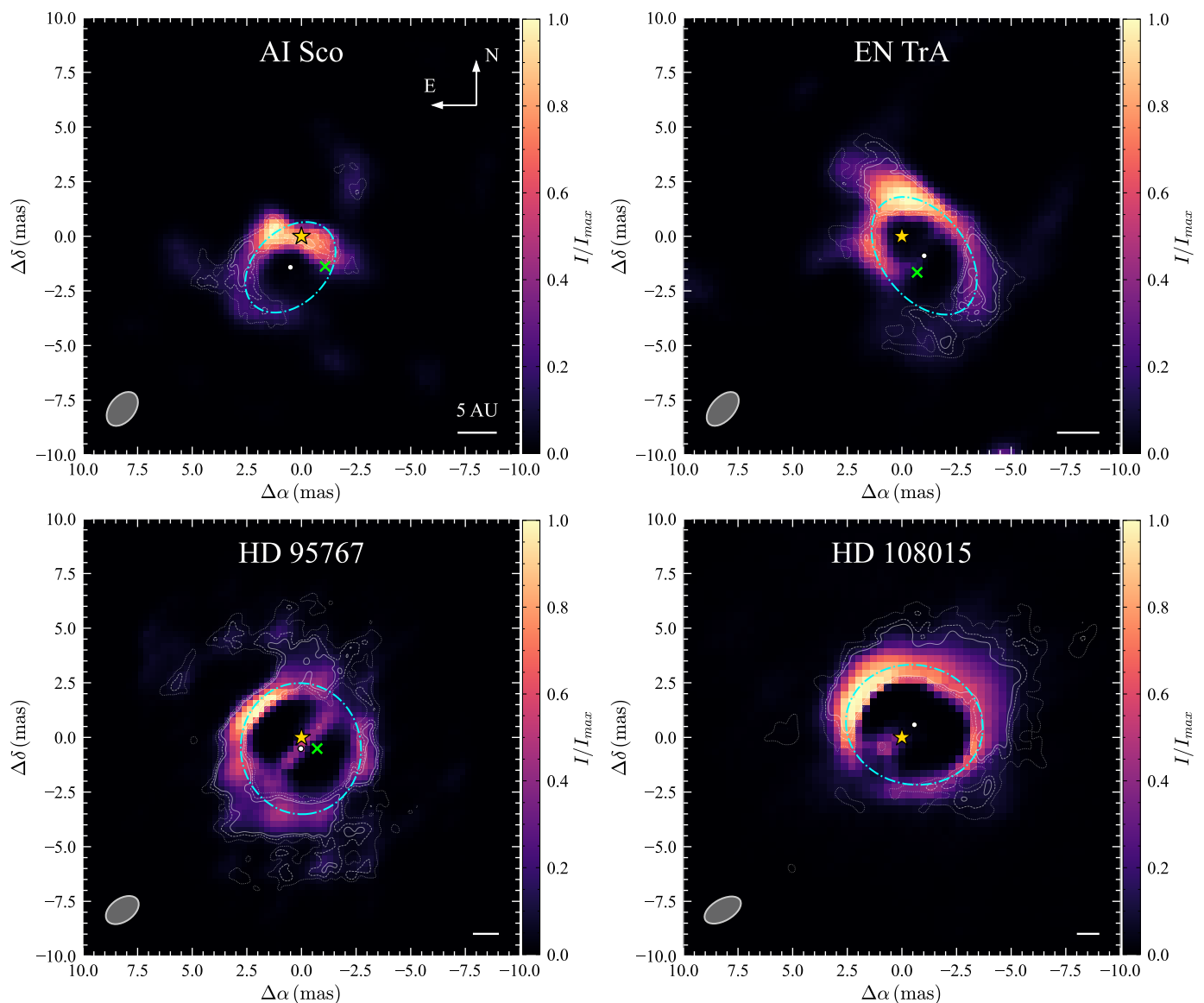


Fig. 3: Peak-normalised ORGanic images for our first four targets (using the image parameters in Table 3). The SPARCO primary and secondary (if detected) are denoted by a golden star and green cross, respectively. The median inner rim fit and the position of its centre (see Table 3) are denoted by a dash-dotted cyan ellipse and a white dot, respectively. 3, 4 and 5 σ contours are given as dotted, dashed and solid white lines. The interferometric beam size and a 5 AU scale bar are shown in the bottom.

5.2. Apparent rim inclinations and the RVb phenomenon

Using PIONIER snapshots, Kluska et al. (2019) performed geometric model fitting of the inner rim and central binary for a large sample of 23 post-AGB circumbinary discs. They found that the apparent inclination of rims observable with PIONIER ranges between $i_{\text{rim}} \sim 10 - 65^\circ$. A significant subset of post-AGB binaries also displays a long-term brightness modulation following the binary period known as the ‘RVb phenomenon’. It is commonly thought to be induced by periodic obscuration along the binary orbit as the line-of-sight to the post-AGB primary grazes the inner rim, and is thus considered to be an indicator of high rim inclination (e.g. Van Winckel et al. 1999; Manick et al. 2017). Nevertheless, Kluska et al. (2019) only found high apparent inclinations ($i_{\text{rim}} \geq 60^\circ$) for three out of nine of their RVb targets, but the authors advised caution when considering their inclination values given the generally poor (u, v) coverage.

The RVb phenomenon has also been firmly established in five out of eight of our targets: AI Sco, HD 95767, HR 4049, IW Car & PS Gem (Table 1). Using our images obtained under greatly superior (u, v) coverage than the snapshots in Kluska et al. (2019), we find moderate apparent inclinations for AI Sco, HR 4049 & IW Car ($45^\circ \lesssim i_{\text{rim}} \lesssim 60^\circ$; Table 3). Moreover, we find low apparent inclinations for HD 95767 and PS Gem ($i_{\text{rim}} \lesssim 30^\circ$; Table 3), though we note their RVb-related V band brightness semi-amplitudes are relatively weak at $\Delta V \lesssim 0.1$ mag (Kiss et al. 2007; Van Winckel et al. 1999). These results corroborate the findings of Kluska et al. (2019), showing that the RVb phenomenon can indeed still occur in the presence of moderate-to-low inclination disc rims. This implies very high disc scale heights in case the conventional disc obscuration hypothesis holds true, and that the exact link between disc rim inclination and the presence of the RVb phenomenon is not yet clear.

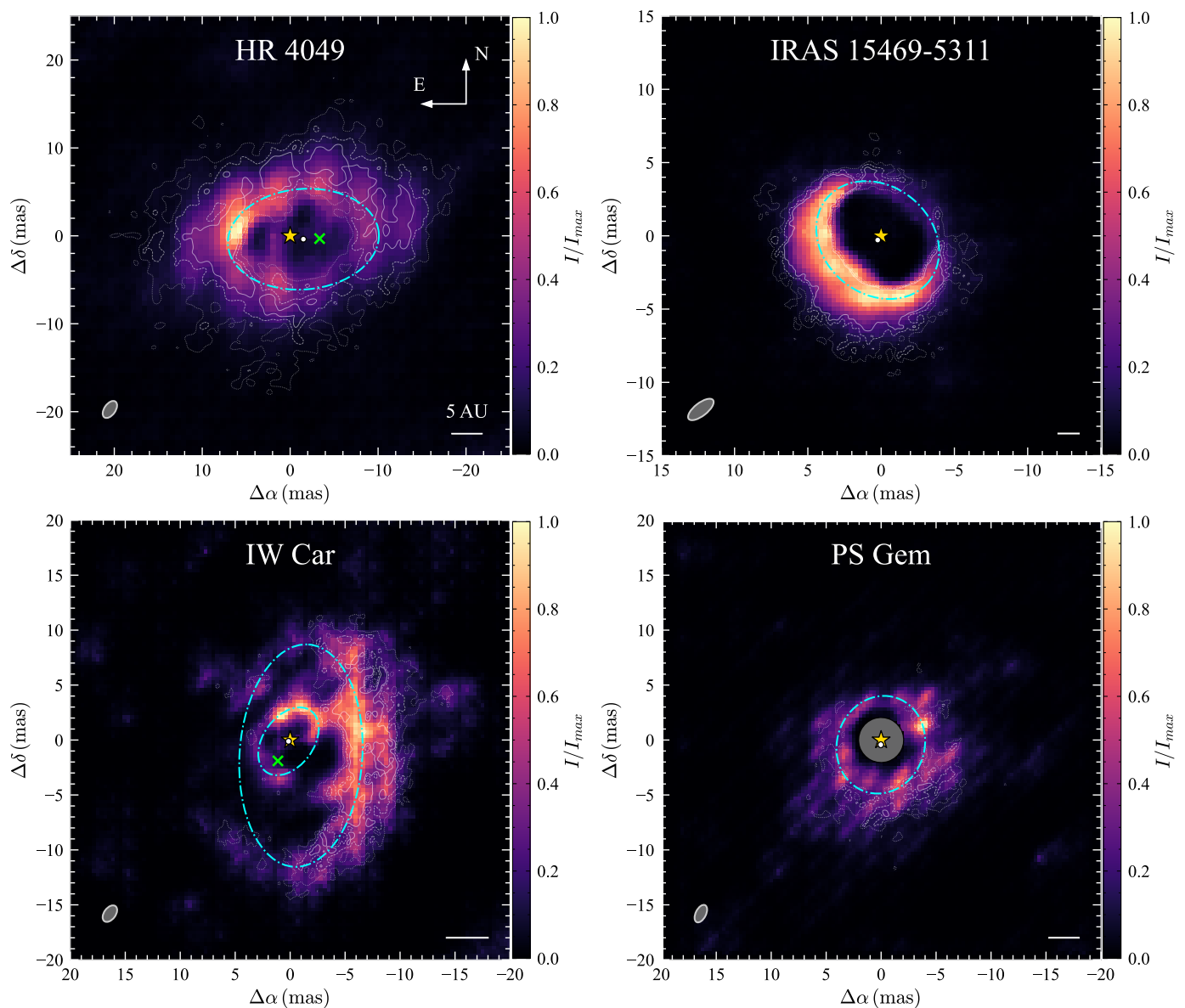


Fig. 4: Analogous to Fig. 3, but for our last four targets. For IW Car, we show inner rim fits for both the inner and outer flux arcs (see Sect. 5.3.7). For the sake of clarity, the rim fit centre is only given for the innermost rim fit. For PS Gem, the strong flux smearing from the primary (see Sect. 5.3.8) has been masked out, as denoted by a grey circle, to better reveal the circumstellar medium.

5.3. Detected features

Below, we describe the detected morphological features in our images, and, when possible, note on connections with features detected in previous studies on the same systems. Especially pertinent in this respect again are the PIONIER snapshot geometric fitting results of Kluska et al. (2019). Since this included all our targets, this enables comparison across a multi-year timebase. We note that this comparison should nevertheless be approached cautiously, as Kluska et al. (2019) used sparse (u, v) coverages and relatively simplistic inner rim models up to only second order in azimuthal modulation. Potential reconstruction artefacts revealed by our tests in Appendices B, D & F are addressed on a case-by-case basis.

5.3.1. AI Sco

Simple RT inclination effects on a smooth, circular rim, centred on a single star, dictate that the NIR emission originates from the far side of the rim relative to the observer. The near side is namely obscured due to self-shadowing, resulting in emission that is antisymmetric relative to the projected rim’s major axis and symmetric relative to the minor one (e.g. Hofmann et al. 2022). While the north-eastern side of AI Sco’s rim is generally brighter than the south-western – likely marking the former as the far side – there is also a strong brightness enhancement towards the primary’s position and the rim’s major axis (Fig. 3). The flux in the immediate vicinity of the primary is also slightly offset southward (by about ~ 1 mas) from where it’s expected to be according to the rim fit. As shown in Appendix B, this is a bias likely induced by the lack of long baseline observations towards the north and north-east (Fig. 1) in combination with the

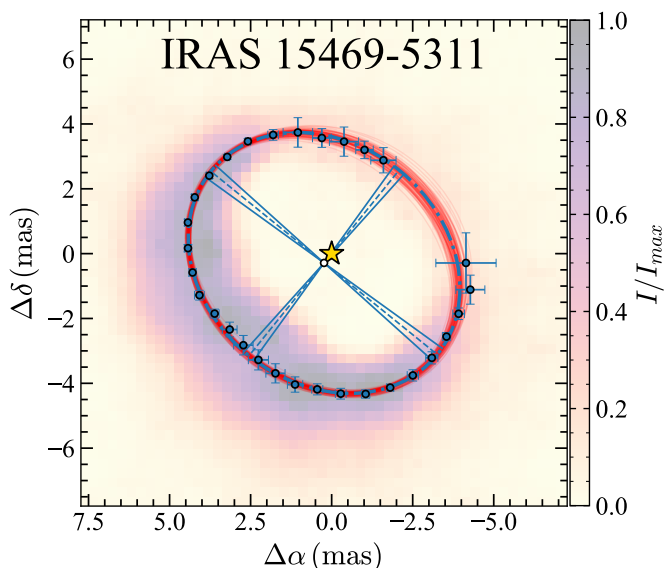


Fig. 5: Example of the inner rim fitting procedure for IRAS 15469-5311. Blue errorbars denote the rim positions along different radial rays. Red ellipses show 100 random samples drawn from the rim’s MCMC chains, with the median ellipse (Table 3) shown in dot-dashed blue. Lines drawn from the median rim centre (white dot) indicate the direction and error of the projected rim’s minor and major axes.

close approach of the primary to the rim. Nevertheless, this morphology cannot be accounted for solely with inclination effects.

The brightness enhancement next to the primary dominates and heavily biases our geometric model towards it, which fails to fully reproduce the fainter ‘tail’ of emission towards the south-east, resulting in a poor goodness-of-fit at $\chi_r^2 \sim 5$ (Fig. B.1 & Table 2). We generally caution that in cases like AI Sco, where the azimuthal brightness profile has sharp features, our simple geometric models with only one order of azimuthal modulation can fail to capture the full complexity and present faulty rim orientations (compare AI Sco’s values in Tables 2 & 3). Nevertheless, the Kluska et al. (2019) model for AI Sco (data taken ~ 5 yr before ours) similarly found a strong brightness enhancement in the direction of the primary (see the model images in their Fig. C.1). This suggests that the bright enhancement could be long-lived, lasting at least several years, and following the primary.

5.3.2. EN TrA

While the inner rim is significantly brighter along the north-western side compared to the south-eastern – suggesting the former represents the far side of the inclined rim – the image cannot be fully explained by just inclination effects (Fig. 3). The rim has a brightness enhancement shifted towards its major axis. This enhancement aligns with the direction of the primary, with both tending towards the north-east side of the rim. The Kluska et al. (2019) geometric model fit (data taken ~ 7 yr before ours) found a brightness enhancement almost symmetric along the north-western side. While this positioning was compatible with disc inclination effects, it also aligned with the direction of the primary at that time. As for AI Sco, the brightness enhancement in our image could last for multiple years and follow the primary.

5.3.3. HD 95767

The inner rim shows a strong brightness enhancement to the north-east, shifted towards its major axis. It could tentatively be aligned with the direction of the primary. The geometric model of Kluska et al. (2019) (data taken ~ 7.5 yr before ours) found the disc to be brightest in the south-east, aligned in the direction of the primary. While suggestive, this should be approached with caution. As shown in Appendix F, the brightness enhancement is highly sensitive to the (u, v) coverage, likely due the combination of a small over- or under-subtraction of the SPARCO secondary together with a particularly high secondary flux fraction ($f_{\text{sec},0} \sim 25\%$, Table 3). Similarly, the small amount of lower per-pixel significance emission in the inner rim cavity is highly likely to be a dirty beam artefact related to the specifics of the (u, v) coverage (see Sect. F.2).

The inner rim emission seems to faintly bulge towards the north and south, with the former curving into an arch-like shape. Although this feature is intriguing, we similarly urge caution in its interpretation, given the high sensitivity of the brightness enhancement and the fact that the dirty beam exhibits a negative flux arch at a comparable location (Fig. F.1). Due to these complications, we exclude HD 95767 from our discussion on potential substructure formation mechanisms further on in Sect. 6.2.

5.3.4. HD 108015

The inner rim is generally brighter along the northern side compared to the southern, suggesting that the former represents the far side of the inclined rim. There is a strong brightness enhancement shifted towards the major axis in the north-east (though there is some uncertainty up to $\sim 10^\circ$ in its position angle; see Appendix D). The primary motion in HD 108015 is not expected to be resolved much at all. Using the spectroscopic value of the primary’s projected semi-major axis, $a_1 \sin i_{\text{bin}}$ (Table 2) and assuming co-planarity between the binary (i.e. $i_{\text{bin}} = i_{\text{rim}}$; Table 3) – a reasonable assumption given that the disc is thought to form from the binary – we estimate $a_1 \sim 0.1$ mas. Hence, the offset between the projected rim centre and primary position is in this case mostly a projection effect due to the fact that the H band continuum is emitted from higher-up regions in the disc (Sect. 5.1). The small amount of flux interior of the cavity towards the south-east is likely an artefact related to the (u, v) coverage (see Appendix F).

It is thus not clear towards which direction of the disc rim the primary is offset. Kluska et al. (2019) (data taken ~ 7.5 yr before ours) instead found a strong brightness enhancement in the south-western sector of the inner rim, approximately opposite of the enhancement we find. If this feature were to be following the primary, given the binary period of 906 ± 6 d and the fact that the orbit is circular (Oomen et al. 2018), we would have expected it to have moved by only $33 \pm 7^\circ$ (calculated between the mean MJD of each observing epoch). Hence, this indicates that the enhancement found in our image is likely moving at its own angular speed, independent of the binary orbit.

5.3.5. HR 4049

The rim is generally brighter along the northern side relative to the southern, marking the former as its far side. A strong brightness enhancement is seen along the eastern side of the rim’s major axis, aligned with the position of the primary. The imaged rim has a slightly choppy appearance, likely caused by the sparser (u, v) coverage along the larger baselines (Fig. 1). While the

western brightness enhancement seems aligned with the primary position, the geometric model by Kluska et al. (2019) (data taken ~ 5 yr before ours) instead shows the main brightness enhancement to also be oriented towards the west, while the primary was oriented east towards a secondary brightness enhancement. As for HD 108015, this tentatively suggests the main brightness enhancement could be long-lived and moving at its own pace, though we do not exclude the possibility that the brightness enhancement is following the primary instead.

5.3.6. IRAS 15469-53110

The rim is brighter along the south-eastern side, marking it as the far side of the inner rim. Furthermore, the rim is highly anti-symmetric along its projected major axis, and simultaneously symmetric along the minor axis. This indicates that the rim morphology, at least at the resolution probed by our observations, is consistent with that of a smooth, inclined circular rim with a centred star, without any other substructure or perturbation.

5.3.7. IW Car

IW Car’s inner disc regions display a highly complex morphology. While a broad outer flux arc is seen to the west, smaller flux arcs are seen closer to the inner binary. These are generally of slightly lower per-pixel significance ($\leq 3\sigma$), yet represent a significant fraction of the total image flux at $12.4 \pm 1.6\%$ ($\sim 4.3 \pm 0.5\%$ of the total flux in H). We note that the exact details of the inner arcs’ azimuthal profile are not fully well-constrained (see Appendix D).

It is not a priori clear whether the outer arc or inner arcs, or perhaps both, represent a bona fide rim structure. As a result, we have applied our rim fitting procedure (Sect. 5.1) to each separately. If both do represent rims, their orientation is likely misaligned, with a difference in inclination and position angle of $\sim 8 \pm 5^\circ$ and $33 \pm 8^\circ$ ($i = 48.5 \pm 5^\circ$ & PA = $144^{+8}_{-7}^\circ$ for the inner arcs and $i = 57 \pm 2^\circ$ & PA = $176 \pm 3^\circ$ for the outer arc; Table 3). Both these orientations are relatively consistent with the orientation of the outer disc found by Andrych et al. (2023) (Fig. 6), using SPHERE/IRDIS H band polarimetric scattered light imaging ($i = 41.7^{+6.5}_{-7.7}^\circ$ & PA = $161^{+12}_{-10}^\circ$; taken ~ 1 yr before our data). This comparison is however complicated by the fact that the outer disc orientation could be biased by artefacts induced during the SPHERE data reduction. Specifically, the inner ‘holes’ due to subtraction of the unresolved polarised flux (Andrych et al. 2023). It is not clear which of the features seen with PIONIER traces the actual inner rim of the outer disc seen by SPHERE.

The geometric fit by Kluska et al. (2019) (data taken ~ 5 yr before ours) recovered the outer flux arc, though it could not capture the inner arcs and the full complexity of the inner disc (as shown by their poorer goodness-of-fit at $\chi^2_\nu = 3.9$).

5.3.8. PS Gem

PS Gem’s image reconstruction shows a very strong flux smearing from the primary (masked in Fig. 4), with a contribution of $\sim 15 \pm 3\%$ to the image flux ($\sim 1.9 \pm 0.3\%$ of the total H band flux). This is likely due to the primary’s orbital movement over the timespan of the observations ($\Delta t_{\text{obs}}/P_{\text{orb}} = 8.7\%$; Table 1), causing it to be better represented as a slightly smeared Gaussian instead of a uniform disc. Its effect is exacerbated by the low flux contribution of the disc at $\sim 13\%$ (causing only

weak non-zero closure phase signal; Fig. E.1) and the strong dirty beam secondary lobes caused by the sparser (u, v) coverage (Figs. 1 & F.1). This causes the retrieved inner rim azimuthal morphology to be very choppy and mostly of low per-pixel significance ($\leq 3\sigma$), though the radial intensity profile is still well-constrained (Fig. 7). While we tentatively discern a bright spot in the west and a broader brightness enhancement in the south of the rim (the latter also being retrieved by our geometric model; Fig. B.1), we forgo including them in our discussion on the origins of potential substructures in Sect. 6.2 due to these complications.

Overall, five out of eight systems show robust, non-axisymmetric brightness features inconsistent with solely inclination effects, indicating that inner rims of post-AGB circumbinary discs are often perturbed.

6. Discussion

In this section, we first examine the mechanisms that determine the inner rim position (Sect. 6.1). We then turn to the possible origins of the robustly detected substructure candidates, drawing heavily on the extensive literature available for protoplanetary discs (Sect. 6.2).

6.1. Mechanism behind the inner rim position

We investigate our detected inner rims in the context of two possible mechanisms setting the rim position: dust sublimation and binary truncation.

6.1.1. Dust sublimation

All our targets exhibit SEDs representative of ‘full’ discs (Kluska et al. 2022), suggesting their energetics are consistent with an inner rim near the dust sublimation radius. To validate this scenario, we confront the derived inner rim radii ($\theta_{\text{rim}}/2$; Table 3) with the expected dust sublimation radius (e.g. Lazareff et al. 2017):

$$R_{\text{sub}} = \frac{1}{2} \left(\frac{C_{\text{bw}}}{\epsilon} \right)^{1/2} \left(\frac{L_*}{4\pi\sigma_{\text{SB}}T_{\text{sub}}^4} \right)^{1/2}, \quad (9)$$

with C_{bw} the backwarming coefficient, ϵ the grain cooling efficiency, L_* the primary’s luminosity (Table 1), σ_{SB} the Stefan-Boltzmann constant and T_{sub} the sublimation temperature. Since R_{sub} and $L_*^{1/2}$ are proportional to the target distance, the angular size of R_{sub} is robust against any errors on the parallax. This includes those induced by the binary motion, as our targets were not marked as astrometric binaries in Gaia DR3.

Kluska et al. (2019) found a typical inner rim temperature of $\sim 1100 - 1400$ K. Meanwhile, Corporaal et al. (2023b) similarly found a rim temperature of ~ 1250 K for the prototypical full disc IRAS 08544-4431 through RT modelling. Given these values, we assume a conservative range of $T_{\text{sub}} = 1000 - 1500$ K. The cooling efficiency reaches its highest value, $\epsilon = 1$, for large grains ($a_{\text{grain}} \gtrsim \lambda_{\text{NIR}}/(2\pi)$; Lazareff et al. 2017). Given that grain growth in post-AGB discs is known to easily proceed up to μm sizes and beyond (e.g. Gielen et al. 2008; Scicluna et al. 2020; Bujarrabal et al. 2023), and the fact that large grains significantly help cool smaller grains even at moderate abundances (Kama et al. 2009), we assume $\epsilon \approx 1$. The backwarming coefficient can take on values of $C_{\text{bw}} = 1 - 4$. The lower limit corresponds to optically thin dust destruction, while the upper corresponds to an instantaneously optically thick, wall-like rim (Kama et al. 2009).

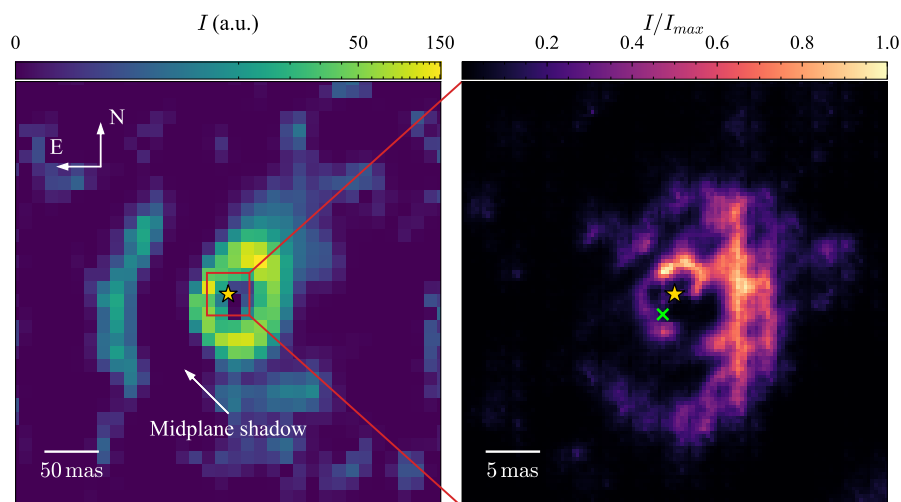


Fig. 6. SPHERE-PIONIER comparison for IW Car. *Left:* SPHERE/IRDIS image (polarised Q_ϕ intensity, adapted from Andrych et al. 2023), probing H band starlight scattered on the outer disc. The image is presented on an arcsinh scale to highlight faint features. The central dark hole is a data reduction artefact due to over-subtraction of the central unresolved polarised flux (Andrych et al. 2023). We mark the midplane’s shadow and the position of the primary. The partial arc to the east likely traces light scattered from the side of the disc facing away from the observer (Andrych et al. 2023). *Right:* zoomed inset with our ORGANIC PIONIER image, probing H band thermal emission in the inner disc regions. The position of the secondary is marked by a green cross.

We show the expected range of dust sublimation radii for $C_{\text{bw}} = 1$ (also accounting for the 1σ uncertainties on L_*) in Fig. 7. Disregarding IW Car, where it is not clear whether the innermost circumstellar flux actually traces the inner rim (see Sect. 6.2.4), the image-derived rim radii lie at or just beyond (~ 1 – 2 mas) the outer edge of the expected $C_{\text{bw}} = 1$ sublimation radii. However, varying the backwarming up to $C_{\text{bw}} = 4$ can raise the R_{sub} estimates by factors of up to two, which can readily provide an excellent match to every target. We conclude that the inner rim positions are compatible with dust sublimation, though most rims are likely not fully optically thin. We also stress that sublimation rims are not well-defined at a single radius. Simulations of PPD sublimation fronts (e.g. Kama et al. 2009; Flock et al. 2016, 2017) instead often display broad, wedge-shaped geometries (extending from $C_{\text{bw}} = 1$ to $C_{\text{bw}} \approx 4$). Unfortunately, the sharpness of the rim is hard to discern from imaging alone, and RT modelling of the SEDs and interferometry (cf. Hillen et al. 2014; Kluska et al. 2018) would be needed to constrain it.

6.1.2. Dynamical truncation by the binary

Alternatively, the location of the inner rim could be set by binary truncation, where resonance torques and non-resonant interactions can carve a cavity in the disc (e.g. Artymowicz & Lubow 1994; Ragusa et al. 2020). Detailed 3D hydrodynamical simulations of circumbinary discs show that binaries can carve cavities with truncation radii of $R_{\text{trunc}} \lesssim 5a$, with a the total binary semi-major axis (though the value decreases with decreasing binary mass ratio and orbital eccentricity, and increasing rim scale height; Hirsh et al. 2020). While we lack full orbital solutions for our targets, we can still set a conservative upper limit on the truncation radius when RV monitoring is available. We do not attempt to use the detected secondary positions, since single astrometric points do not provide strong enough constraints on the orbital parameters, and dedicated astrometric modelling would be required for this purpose (e.g. Anugu et al. 2023).

First, the spectroscopic mass function of the secondary, $f(m)$, can be rewritten as follows:

$$f(m) = \frac{M_{\text{sec}}^3}{(M_{\text{prim}} + M_{\text{sec}})^2} \sin^3 i_{\text{bin}} = \frac{M_{\text{prim}}}{a^2(a - a_1)} (a_1 \sin i_{\text{bin}})^3. \quad (10)$$

As we did for HD 108015 in Sect. 5.3.4, we assume co-planarity between the disc rim and the binary (i.e. $i_{\text{bin}} = i_{\text{rim}}$; Table 3).

Following Oomen et al. 2018, we assume the post-AGB primary to follow the mass distribution of single white dwarfs in the Galactic field. Specifically, we adopt the value of $M_{\text{prim}} = 0.62 \pm 0.11 M_\odot$ from Tremblay et al. 2016. If the values of $a_1 \sin i_{\text{bin}}$ and $f(m)$ are available from RV monitoring (Table 1), Eq. 10 can readily be solved for the total semi-major axis a . The upper limit for the binary truncation radius inferred from this ($R_{\text{trunc}} \lesssim 5a$) is displayed for our targets with previous RV monitoring on Fig. 7. We find that the inner rims of HD 108015, HR 4049 and IRAS 15469-5311 are highly unlikely to be set through tidal truncation, and are mostly unaffected by torque from the binary. Without tighter constraints on the binary orbital properties and rim scale height, we cannot make such assumptions for the other targets, and the inner rim might be set either by binary truncation or by sublimation physics.

6.2. Origins of the detected potential substructures

We identified several robust brightness asymmetries from our images in Sect. 5.3. Most strikingly, we found a number of brightness enhancements along the inner rim, not symmetric with the rim minor axis and inconsistent with inclination effects. For IW Car, the image reconstruction revealed an even more puzzling morphology, finding inner flux arcs seemingly misaligned with a large, outer flux arc to the west. We will now address several physical mechanisms that could lie at the origin of these features, as well as possible ways to discern them. We stress that while we are sensitive to thermal emission from small grains well-coupled to the gas, the emission can be optically thick (e.g. Hillen et al. 2014; Kluska et al. 2019; Corporaal et al. 2023b). As a result, relating the brightness contrasts of features seen in the images (Figs. 3 & 4) to gas density enhancements predicted by mechanisms mentioned below is outside the scope of this work.

6.2.1. Thermal response to the primary’s orbit

Comparing with the geometric PIONIER snapshot modelling study of Kluska et al. (2019), we found that the azimuthal brightness enhancement in AI Sco, EN TrA & HR 4049 (Sects. 5.3.1, 5.3.2 & 5.3.3) might be long-lived and following the movement of the primary star. We propose that the irradiation of the primary can preferentially heat parts of the disc rim it is closest to, locally increasing the temperature, scale height and brightness. Indeed, a similar mechanism was previously invoked to explain the

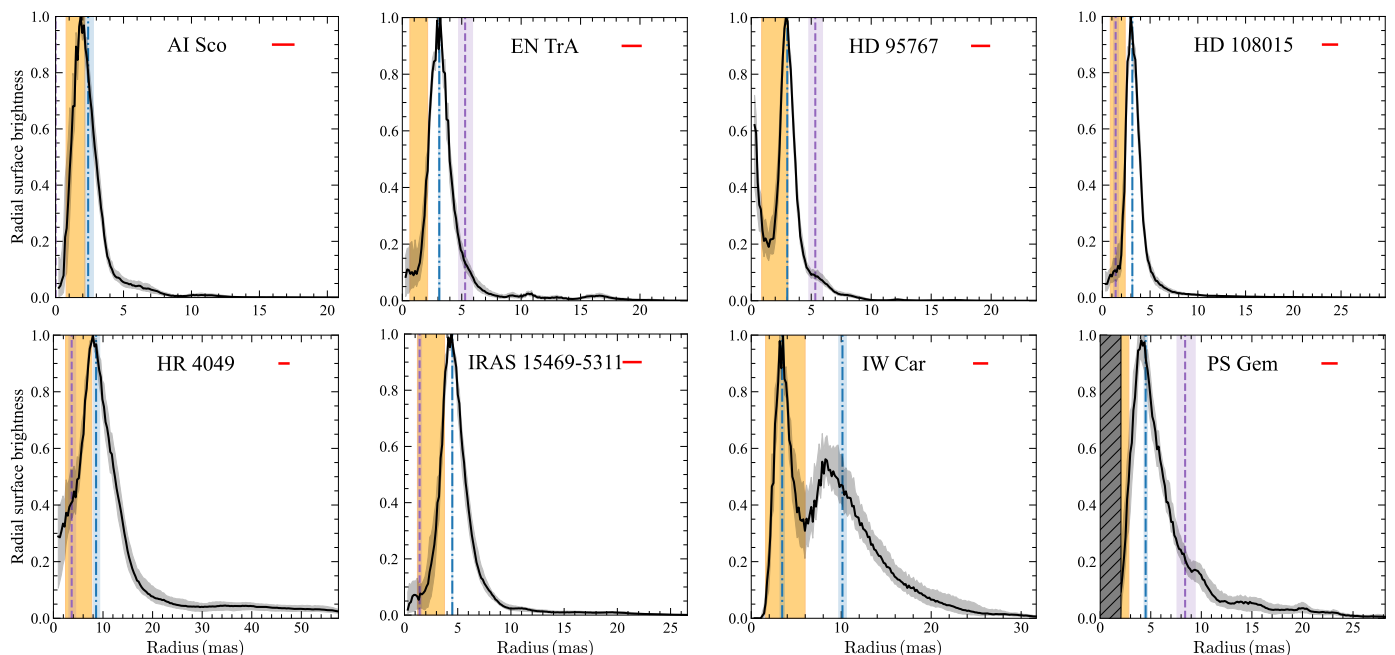


Fig. 7: Peak-normalised ORGanic radial surface brightness profiles. The profiles and their 1σ contours are given in black, with red bars denoting the azimuthally averaged beam size. An orange strip represents the range of sublimation radii for $C_{\text{bw}} = 1$ (Sect. 6.1.1). The image-derived inner rim radius ($\theta_{\text{rim}}/2$; Table 3) is given as dot-dashed blue line, and for targets where RV monitoring is available (Table 1), a dashed purple line provides an upper limit to the binary truncation radius R_{trunc} (Sect. 6.1.2). Shaded regions indicate 1σ errors for both. For IW Car, we display inner rim radii for both the inner and outer flux arcs (see Sect. 5.3.7), with the brightness profile calculation based on the orientation of the inner arcs. For PS Gem, a mask was placed in front of the primary to mitigate the effects of strong flux smearing (Sect. 5.3.8), as denoted by a hatched strip.

MIR variability of the circumbinary PPD CoKu TAU/4, showing that the thermal response of the inner rim is almost instant relative to the binary motion for typical density and temperature values (Nagel et al. 2010). This was also cautiously considered by Kluska et al. (2018) as an explanation for the rim brightness enhancement in the post-AGB disc IRAS 08544-4431.

If this mechanism is indeed active for post-AGB circumbinary discs, these brightness enhancements should follow the primary’s position along its orbit. While comparison of our images with the modelling results of Kluska et al. (2019) is strongly suggestive of this, the complexity of the retrieved morphologies necessitates multi-epoch imaging to fully confirm this scenario.

6.2.2. Dynamical interaction with the binary

Ragusa et al. (2020) performed comprehensive 3D hydrodynamical simulations for co-planar binary-truncated discs, showing that the inner rim becomes eccentric – even for circular binaries – at mass ratios $q \geq 0.05$. This criterion is easily fulfilled by our targets (Oomen et al. 2018). The simulations show two simultaneously occurring types of substructure. First, a long-lived crescent-like gas density enhancement at the eccentric rim, caused by a ‘traffic jam’, as the orbits of the gas are squeezed due to gradients in disc eccentricity (Ataiee et al. 2013). Second, a co-moving overdensity for mass ratios $q \geq 0.2$, possibly formed by gas streams launched across the cavity (e.g. Shi et al. 2012; Ragusa et al. 2017; Calcino et al. 2019). Under our currently limited constraints on the central binary orbit and disc rim scale height, these substructure formation mechanisms could potentially be active in all our targets except HD 108015, HR 4049 and IRAS 15469-5311 (where the rim is unlikely to be affected

by binary torque; Sect. 6.1.2). AI Sco is a particularly enticing candidate for these mechanisms, since the binary stars closely approach the rim, and the apparent rim centre is heavily displaced in the direction of the projected major axis relative to the binary, potentially indicating an eccentric disc cavity (Fig. 3).

These binary-induced substructures are readily discernable from both each other and a thermal response to the primary through their expected motion. Features caused by thermal response should orbit on a timescale of P_{orb} (Table 1), while the binary-induced traffic jam and co-moving overdensity are, respectively, precessing on a timescale of $\sim 100 - 1000 P_{\text{orb}}$ and orbiting with the local Keplerian velocity (Ragusa et al. 2020). This clear separation in expected motion provides a powerful way of discriminating between thermal and dynamical origins.

6.2.3. Hydrodynamical instability

Another possible mechanism causing asymmetric structure in inner disc rims is hydrodynamical instability. Specifically, the Rossby wave instability (RWI; e.g. Lovelace et al. 1999; Meheut et al. 2013; Bae et al. 2023). RWI occurs when there is a local maximum in the vortensity of the disc, typically induced by an initial bump in the gas pressure. If local viscosity is low, the disc can form a single, long-lived vortex, orbiting at approximately the local Keplerian velocity (Lyra & Mac Low 2012; Meheut et al. 2012). While there are currently no constraints on the vortensity or viscosity in our target discs – there being only a single constraint on viscosity via RT modelling of the full post-AGB disc IRAS 08544-4431 (Kluska et al. 2018; Corporaal et al. 2023b) – RWI provides a physically motivated framework for producing long-lived azimuthal asymmetries at the rim moving

at timescales different from the binary. The brightness enhancements we find for HD 108015 and HR 4049 are possibly moving separately from the primary (Sects. 5.3.4 & 5.3.5), and are likely unaffected by binary torque (Sect. 6.1.2). This makes them consistent with a possible vortex scenario.

Several ways of inducing such initial pressure bumps are considered for PPDs. One such scenario is the carving of gaps and cavities by massive planets (e.g. Pinilla et al. 2012). Nevertheless, despite their status as potential second-generation planet formation sites (Kluska et al. 2022), no candidate planet detections in post-AGB discs have been made so far. A scenario that does not invoke the presence of planets are turbulent ‘dead zones’. A dead zone pressure bump occurs in discs where accretion is mediated by the magnetorotational instability (MRI; Balbus & Hawley 1998), as gas transitions from ionised to non-ionised and MRI turbulence becomes quiescent (e.g. Flock et al. 2016; Flock et al. 2019). Previous work on PPDs showed that thermal ionisation alone is sufficient to produce strong ionisation transitions around ~ 1000 K (e.g. Desch & Turner 2015; Jankovic et al. 2021), positioning the resulting pressure bump and RWI vortex close to the silicate sublimation rim (e.g. Flock et al. 2017).

If RWI operates in the inner rim, the bright region should orbit at the local Keplerian velocity. It would be readily discernable with multi-epoch imaging from the other formation mechanisms considered here, except the binary-induced co-moving overdensities. Both types of feature namely move at similar angular speeds, and resolving their subtle kinematic differences (a lack of vorticity in the binary-induced overdensities) is beyond the capabilities of current facilities.

6.2.4. IW Car: a morphological puzzle

The inner disc of IW Car shows a highly complex morphology (Sect. 5.3.7). A large flux arc is seen to the west, with additional smaller inner flux arcs found closer to the binary (Fig. 4).

The large western flux arc might trace the inner rim of the outer disc probed by SPHERE (Fig. 6). The inner arcs could then probe accretion streams from the western rim onto the binary, with the emission originating from either hot, optically thick gas (e.g. Kraus et al. 2008), or specific refractory dust grains which can survive at higher temperatures inward of the main rim (e.g. corundum or iron; Kama et al. 2009). Alternatively, if both the western arc and the inner arcs represent rim-like structures, the two are likely misaligned relative to each other (Sect. 5.3.7 & Table 3). This could be accounted for by a warped innermost disc (Facchini et al. 2013), which was recently put forward to explain morphological differences between visual and NIR images of the outer disc of the post-AGB binary IRAS 08544-4431 (Andrych et al. 2024). Such warps can be induced by initial inclination misalignments between the binary orbit and the disc (e.g. Young et al. 2023), or by the presence of an embedded giant planet on an inclined orbit (Nealon et al. 2018).

In case the inner arcs trace the actual inner rim of the outer disc observed with SPHERE (Fig. 6), the large western arc possibly traces a loosely wound spiral-like feature. This can explain why the western flux arc seemingly attaches to the inner flux arcs north-west of the primary (Fig. 4). Spiral arms can be induced in the disc by the presence of an embedded giant planet, which should co-move with the orbit of their perturber (e.g. Dong et al. 2015; Ren et al. 2020). They may also be induced in an outflow lofted above the disc, similar to the putative secondary condensation front previously found for the full post-AGB disc HD 101584 (Kluska et al. 2020b). Gravitational

interaction with the binary is also a possibility, though the resulting spirals are typically more flocculent and highly wound (e.g. Price et al. 2018).

Additional imaging epochs are needed to disentangle these interpretations. Such observations could confirm if the inner arcs are transient accretion streams or represent a stable rim structure, and whether the western flux arc is static and indicative of a rim structure, or moving and indicative of a dynamical spiral.

7. Summary and conclusions

This study aimed to reveal the morphological complexity of the inner regions in a varied sample of post-AGB circumbinary discs by spatially resolving them. To this end, we have successfully introduced a consistent image reconstruction workflow, combining the SPARCO approach with the ORGANIC reconstruction and BADS optimisation algorithms. We applied this workflow to VLT/PIONIER observations of eight diverse full disc targets, obtained under the INSPIRING ESO large programme, providing the first homogeneous, high fidelity imaging survey of the inner disc regions.

Our images clearly resolve the inner disc regions for all targets. The dusty inner rim sizes are generally compatible with dust sublimation, under the condition that the rims are not always fully optically thin. The possibility that the rim is set by binary tidal truncation instead cannot be excluded except for three targets – HD 108015, HR 4049 & IRAS 15469-5311. Further constraints on the binary properties (e.g. combining RV monitoring with relative interferometric astrometry), ideally in addition with constraints on the inner rim height from RT modelling, would clarify whether discs could be binary-truncated on a system-by-system basis.

The images reveal a high degree of morphological complexity, displaying asymmetric azimuthal brightness enhancements that are significantly shifted way from the minor projected rim axis. After extensive testing of the image robustness, we demonstrate that the overall structure and orientation of these brightness enhancements is reliable in four targets – though finer details of the azimuthal profile, such as small-scale clumpiness, can be affected by artefacts and specifics of the imaging routine (Appendices B & D). These enhancements are inconsistent with brightness asymmetry induced by simple RT effects of an inclined, smooth circular rim surrounding a single star. Only one target’s image – IRAS 15469-5311 – can be fully accounted for by invoking just inclination effects. Comparison with the results of the PIONIER snapshot geometric modelling study by Kluska et al. (2019), providing a multi-year timebase with respect to our observations, tentatively suggests these brightness enhancements could be long-lived and moving. They likely either follow the position of the primary star or move at an angular speed independent of the binary. Nevertheless, given the poor (u, v) coverage in the Kluska et al. (2019) study, follow-up imaging is needed to fully confirm these scenarios. One target – IW Car – shows a large outer flux arc to the west, as well as smaller inner flux arcs close to the central binary.

Drawing on the extensive literature available for PPDs, various substructure formation mechanisms able to explain these features are considered. A thermal response of the inner rim to the variable irradiation of the primary as it orbits provides a natural explanation for brightness enhancements following the primary. In cases where the inner rim is set by binary truncation, slowly precessing, crescent-like features as well as co-moving overdensities can be produced. Co-moving vortices induced by RWI also form a strong contender for features mov-

ing independent of the binary. These could occur at gaps and cavities carved by massive planets or at magnetic dead zones close to the sublimation radius. Given the different expected rates of angular movement for these mechanisms, time-series imaging would provide a strong means of both fully establishing their presence and discerning amongst them. Only RWI vortices and binary-induced overdensities would be hard to disentangle, since both substructures co-move at the local Keplerian velocity. For IW Car the inner flux arcs could represent either accretion streams onto the central stars or a slightly warped innermost disc, with the large western arc denoting the disc rim. Alternatively, the inner arcs might probe the main disc rim, and the western arc a spiral-like feature located in the disc or in an outflow. The extent to which these features can affect the general disc structure and spatial distribution of gas and dust – like the ubiquitous refractory depletion, potentially suspected to be induced by dust trapping substructures (e.g. Oomen et al. 2019; Kluska et al. 2022; Mohorian et al. 2024) – remains to be explored.

Future time-resolved and multi-wavelength imaging campaigns, including MIR observations with VLTI/MATISSE and (sub)-mm observations with ALMA, will allow us to probe more radially extended and vertically deeper disc regions, as well as produce the first inner rim images for transition disc targets. This will provide the temporal and spectral leverage needed to fully unveil the dynamics of these complex environments. Dedicated modelling of substructure formation scenarios would then be called for in order to fully uncover their implications with regards to refractory depletion, possible second-generation planet formation or changes to the orbital architecture of any surviving first-generation planets.

Data availability

Observation logs for the selected VLTI/PIONIER observations are publicly available on Zenodo: <https://doi.org/10.5281/zenodo.20155601>.

Acknowledgements. TDP acknowledges support of the Research Foundation - Flanders (FWO) under grant 11P6I24N. DK, HVW, and KA acknowledge the support of the Australian Research Council through Discovery Project DP240101150. JA and VB acknowledge the financial support of the project CRISPNESS, grant PID2023-146056NB-C21, funded by MICIU/AEI/10.13039/501100011033 and by ERDF/EU. SK acknowledges support from an ERC Consolidator Grant (Grant Agreement ID 101003096) and STFC Small Award (ST/Y002695/1). This research has made use of the SIMBAD database, operated at CDS, Strasbourg, France. This work was performed on the OzSTAR national facility at Swinburne University of Technology. The OzSTAR program receives funding in part from the Astronomy National Collaborative Research Infrastructure Strategy (NCRIS) allocation provided by the Australian Government, and from the Victorian Higher Education State Investment Fund (VHESIF) provided by the Victorian Government. This research has made use of the Jean-Marie Mariotti Center OiDB service. This research has made use of the PIONIER data reduction package of the Jean-Marie Mariotti Center. This research has made use of the Jean-Marie Mariotti Center SearchCal service, which involves the JSDC and JMDC catalogues.

References

Acerbi, L. & Ma, W. J. 2017, in *Advances in Neural Information Processing Systems*, ed. I. Guyon, U. V. Luxburg, S. Bengio, H. Wallach, R. Fergus, S. Vishwanathan, & R. Garnett, Vol. 30 (Curran Associates, Inc.)
 Andrews, S. M., Huang, J., Pérez, L. M., et al. 2018, *ApJ*, 869, L41
 Andrych, K., Kamath, D., Kluska, J., et al. 2023, *MNRAS*, 524, 4168
 Andrych, K., Kamath, D., Van Winckel, H., et al. 2025, *PASA*, 1–36
 Andrych, K., Kamath, D., Van Winckel, H., et al. 2024, *MNRAS*, 535, 1763
 Anugu, N., Kluska, J., Gardner, T., et al. 2023, *ApJ*, 950, 149
 Arjovsky, M. & Bottou, L. 2017, *arXiv e-prints*, arXiv:1701.04862
 Arjovsky, M., Chintala, S., & Bottou, L. 2017, *arXiv e-prints*, arXiv:1701.07875

Artymowicz, P. & Lubow, S. H. 1994, *ApJ*, 421, 651
 Ataiee, S., Pinilla, P., Zsom, A., et al. 2013, *A&A*, 553, L3
 Bae, J., Isella, A., Zhu, Z., et al. 2023, in *Astronomical Society of the Pacific Conference Series*, Vol. 534, *Protostars and Planets VII*, ed. S. Inutsuka, Y. Aikawa, T. Muto, K. Tomida, & M. Tamura, 423
 Bailer-Jones, C. A. L., Rybizki, J., Founesneau, M., Demleitner, M., & Andrae, R. 2021, *AJ*, 161, 147
 Balbus, S. A. & Hawley, J. F. 1998, *Rev. Mod. Phys.*, 70, 1
 Baron, F., Monnier, J. D., & Kloppenborg, B. 2010, in *Society of Photo-Optical Instrumentation Engineers (SPIE) Conference Series*, Vol. 7734, *Optical and Infrared Interferometry II*, ed. W. C. Danchi, F. Delplancke, & J. K. Rajagopal, 77342I
 Bertolami, M. M. M. 2016, *A&A*, 588, A25
 Bollen, D., Kamath, D., Van Winckel, H., et al. 2022, *A&A*, 666, A40
 Bujarrabal, V., Alcolea, J., Van Winckel, H., Santander-García, M., & Castro-Carrizo, A. 2013a, *A&A*, 557, A104
 Bujarrabal, V., Alcolea, J., Castro-Carrizo, A., et al. 2023, *A&A*, 677, L18
 Bujarrabal, V., Castro-Carrizo, A., Alcolea, J., & Van Winckel, H. 2015, *A&A*, 575, L7
 Bujarrabal, V., Castro-Carrizo, A., Alcolea, J., et al. 2017, *A&A*, 597, L5
 Bujarrabal, V., Castro-Carrizo, A., Van Winckel, H., et al. 2018, *A&A*, 614, A58
 Bujarrabal, V., Castro-Carrizo, A., Alcolea, J., et al. 2013b, *A&A*, 557, L11
 Calcino, J., Price, D. J., Pinte, C., et al. 2019, *MNRAS*, 490, 2579
 Chelli, A., Duvert, G., Bourgeès, L., et al. 2016, *A&A*, 589, A112
 Claes, R., Kluska, J., Winckel, H. V., & Min, M. 2020, in *Optical and Infrared Interferometry and Imaging VII*, ed. P. G. Tuthill, A. Mérand, & S. Sallum, Vol. 11446, *International Society for Optics and Photonics (SPIE)*, 114461U
 Corporaal, A., Kluska, J., Van Winckel, H., et al. 2023a, *A&A*, 674, A151
 Corporaal, A., Kluska, J., Van Winckel, H., Kamath, D., & Min, M. 2023b, *A&A*, 671, A15
 de Boer, J., Salter, G., Benisty, M., et al. 2016, *A&A*, 595, A114
 De Prins, T., Van Winckel, H., Ferreira, J., et al. 2024, *A&A*, 689, A151
 de Ruiter, S., van Winckel, H., Maas, T., et al. 2006, *A&A*, 448, 641
 Desch, S. J. & Turner, N. J. 2015, *ApJ*, 811, 156
 Dong, R., Zhu, Z., Rafikov, R. R., & Stone, J. M. 2015, *ApJ*, 809, L5
 Drevon, J., Millour, F., Cruzalèbes, P., et al. 2024, *MNRAS*, 527, L88
 Efron, B. 1979, *The Annals of Statistics*, 7, 1
 Ertel, S., Kamath, D., Hillen, M., et al. 2019, *AJ*, 157, 110
 Facchini, S., Lodato, G., & Price, D. J. 2013, *MNRAS*, 433, 2142
 Flock, M., Fromang, S., Turner, N. J., & Benisty, M. 2016, *ApJ*, 827, 144
 Flock, M., Fromang, S., Turner, N. J., & Benisty, M. 2017, *ApJ*, 835, 230
 Flock, M., Turner, Neal J., Mulders, Gijs D., et al. 2019, *A&A*, 630, A147
 Foreman-Mackey, D., Hogg, D. W., Lang, D., & Goodman, J. 2013, *PASP*, 125, 306
 Gallardo Cava, I., Gómez-Garrido, M., Bujarrabal, V., et al. 2021, *A&A*, 648, A93
 Garufi, A., Ginski, C., van Holstein, R. G., et al. 2024, *A&A*, 685, A53
 Gewers, F. L., Ferreira, G. R., Arruda, H. F. D., et al. 2021, *ACM Comput. Surv.*, 54
 Gielen, C., Van Winckel, H., Min, M., Waters, L. B. F. M., & Lloyd Evans, T. 2008, *A&A*, 490, 725
 Giridhar, S., Lambert, D. L., & Gonzalez, G. 1998, *ApJ*, 509, 366
 Giridhar, S., Lambert, D. L., Reddy, B. E., Gonzalez, G., & Yong, D. 2005, *ApJ*, 627, 432
 Giridhar, S., Rao, N. K., & Lambert, D. L. 1994, *ApJ*, 437, 476
 Goodfellow, I. J., Pouget-Abadie, J., Mirza, M., et al. 2014, *arXiv e-prints*, arXiv:1406.2661
 Gorlova, N., Van Winckel, H., Gielen, C., et al. 2012, *A&A*, 542, A27
 GRAVITY Collaboration, Perraut, K., Labadie, L., et al. 2019, *A&A*, 632, A53
 Haguenaue, P., Alonso, J., Bourget, P., et al. 2010, in *Optical and Infrared Interferometry II*, Vol. 7734 (SPIE), 773404
 Hillen, M., de Vries, B. L., Menu, J., et al. 2015, *A&A*, 578, A40
 Hillen, M., Kluska, J., Le Bouquin, J.-B., et al. 2016, *A&A*, 588, L1
 Hillen, M., Menu, J., Van Winckel, H., et al. 2014, *A&A*, 568, A12
 Hillen, M., Van Winckel, H., Menu, J., et al. 2017, *A&A*, 599, A41
 Hirsh, K., Price, D. J., Gonzalez, J.-F., Ubeira-Gabellini, M. G., & Ragusa, E. 2020, *MNRAS*, 498, 2936
 Hofmann, K.-H., Bensberg, A., Schertl, D., et al. 2022, *A&A*, 658, A81
 Ibrahim, N., Monnier, J. D., Kraus, S., et al. 2023, *ApJ*, 947, 68
 Jankovic, M. R., Owen, J. E., Mohanty, S., & Tan, J. C. 2021, *MNRAS*, 504, 280
 Kama, M., Folsom, C. P., & Pinilla, P. 2015, *A&A*, 582, L10
 Kama, M., Min, M., & Dominik, C. 2009, *A&A*, 506, 1199
 Kamath, D., Wood, P. R., & Van Winckel, H. 2014, *MNRAS*, 439, 2211
 Kamath, D., Wood, P. R., & Van Winckel, H. 2015, *MNRAS*, 454, 1468
 Kipper, T. 2013, *Baltic Astronomy*, 22, 101
 Kiss, L. L. & Bódi, A. 2017, *A&A*, 608, A99
 Kiss, L. L., Derekas, A., Szabó, G. M., Bedding, T. R., & Szabados, L. 2007, *MNRAS*, 375, 1338
 Kluska, J., Benisty, M., Soulez, F., et al. 2016, *A&A*, 591, A82
 Kluska, J., Berger, J.-P., Malbet, F., et al. 2020a, *A&A*, 636, A116

- Kluska, J., Hillen, M., Van Winckel, H., et al. 2018, *A&A*, 616, A153
- Kluska, J., Malbet, F., Berger, J.-P., et al. 2014, *A&A*, 564, A80
- Kluska, J., Olofsson, H., Van Winckel, H., et al. 2020b, *A&A*, 642, A152
- Kluska, J., Van Winckel, H., Coppée, Q., et al. 2022, *A&A*, 658, A36
- Kluska, J., Van Winckel, H., Hillen, M., et al. 2019, *A&A*, 631, A108
- Kraus, S., Preibisch, T., & Ohnaka, K. 2008, *ApJ*, 676, 490
- Lazareff, B., Berger, J.-P., Kluska, J., et al. 2017, *A&A*, 599, A85
- Le Bouquin, J.-B., Berger, J.-P., Lazareff, B., et al. 2011, *A&A*, 535, A67
- Levis, A., Chael, A. A., Bouman, K. L., Wielgus, M., & Srinivasan, P. P. 2024, *Nature Astronomy*, 8, 765
- Lilley, L., Norris, B., Tuthill, P., et al. 2026, *Journal of Astronomical Telescopes, Instruments, and Systems*, 12, 018001
- Lloyd, S. 1982, *IEEE Transactions on Information Theory*, 28, 129
- Lovelace, R. V. E., Li, H., Colgate, S. A., & Nelson, A. F. 1999, *ApJ*, 513, 805
- Lucas, M., Norris, B., Guyon, O., et al. 2024, *PASP*, 136, 114504
- Lyra, W. & Mac Low, M.-M. 2012, *ApJ*, 756, 62
- Maas, T., Van Winckel, H., & Lloyd Evans, T. 2005, *A&A*, 429, 297
- Manick, R., Van Winckel, H., Kamath, D., Hillen, M., & Escorza, A. 2017, *A&A*, 597, A129
- Marquardt, D. W. 1963, *Journal of the Society for Industrial and Applied Mathematics*, 11, 431
- Meheut, H., Keppens, R., Casse, F., & Benz, W. 2012, *A&A*, 542, A9
- Meheut, H., Lovelace, R. V. E., & Lai, D. 2013, *MNRAS*, 430, 1988
- Mérand, A. 2022, in *Optical and Infrared Interferometry and Imaging VIII*, ed. A. Mérand, S. Sallum, & J. Sanchez-Bermudez, Vol. 12183, International Society for Optics and Photonics (SPIE), 121831N
- Min, M., Dullemond, C. P., Dominik, C., de Koter, A., & Hovenier, J. W. 2009, *A&A*, 497, 155
- Mohorian, M., Kamath, D., Menon, M., et al. 2025, *MNRAS*, 538, 1339
- Mohorian, M., Kamath, D., Menon, M., et al. 2024, *MNRAS*, 530, 761
- Monnier, J. D., Che, X., Zhao, M., et al. 2012, *ApJS*, 761, L3
- Nagel, E., D'Alessio, P., Calvet, N., et al. 2010, *ApJ*, 708, 38
- Nealon, R., Dipierro, G., Alexander, R., Martin, R. G., & Nixon, C. 2018, *MNRAS*, 481, 20
- Oomen, G.-M., Van Winckel, H., Pols, O., et al. 2018, *A&A*, 620, A85
- Oomen, G.-M., Van Winckel, H., Pols, O., Onno, & Nelemans, G. 2019, *A&A*, 629, A49
- Pinilla, P., Benisty, M., & Birnstiel, T. 2012, *A&A*, 545, A81
- Pinte, C., Harries, T. J., Min, M., et al. 2009, *A&A*, 498, 967
- Pinte, C., Ménard, F., Duchêne, G., & Bastien, P. 2006, *A&A*, 459, 797
- Planquart, L., Paladini, C., Jorissen, A., et al. 2024, *A&A*, 687, A306
- Price, D. J., Cuello, N., Pinte, C., et al. 2018, *MNRAS*, 477, 1270
- Ragusa, E., Alexander, R., Calcino, J., Hirsh, K., & Price, D. J. 2020, *MNRAS*, 499, 3362
- Ragusa, E., Dipierro, G., Lodato, G., Laibe, G., & Price, D. J. 2017, *MNRAS*, 464, 1449
- Rao, S. S. & Giridhar, S. 2014, *Rev. Mexicana Astron. Astrofis.*, 50, 49
- Rasmussen, C. E. & Williams, C. K. I. 2006, *Gaussian Processes for Machine Learning* (The MIT Press)
- Ren, B., Dong, R., van Holstein, R. G., et al. 2020, *ApJ*, 898, L38
- Renard, S., Thiébaud, E., & Malbet, F. 2011, *A&A*, 533, A64
- Rudin, L. I., Osher, S., & Fatemi, E. 1992, *Physica D Nonlinear Phenomena*, 60, 259
- Sahai, R., Claussen, M. J., Schnee, S., Morris, M. R., & Sánchez Contreras, C. 2011, *ApJ*, 739, L3
- Schwarz, G. 1978, *Annals of Statistics*, 6, 461
- Scicluna, P., Kemper, F., Trejo, A., et al. 2020, *MNRAS*, 494, 2925
- Setterholm, B. R., Monnier, J. D., Baron, F., et al. 2025, *AJ*, 169, 318
- Shi, J.-M., Krolik, J. H., Lubow, S. H., & Hawley, J. F. 2012, *ApJ*, 749, 118
- Singh, G. S. & Acerbi, L. 2024, *Journal of Open Source Software*, 9, 5694
- Thiébaud, E. & Young, J. 2017, *J. Opt. Soc. Am. A*, 34, 904
- Tremblay, P.-E., Cummings, J., Kalirai, J. S., et al. 2016, *MNRAS*, 461, 2100
- Ulyanov, D., Vedaldi, A., & Lempitsky, V. 2020, *International Journal of Computer Vision*, 128, 1867–1888
- Van Winckel, H. 1997, *A&A*, 319, 561
- Van Winckel, H. 2003, *ARA&A*, 41, 391
- Van Winckel, H. 2019, in *The Impact of Binary Stars on Stellar Evolution* (Cambridge University Press), 92–105
- Van Winckel, H. 2025, *Galaxies*, 13, 68
- Van Winckel, H., Lloyd Evans, T., Briquet, M., et al. 2009, *A&A*, 505, 1221
- Van Winckel, H., Waelkens, C., Fernie, J. D., & Waters, L. B. F. M. 1999, *A&A*, 343, 202
- Van Winckel, H., Waelkens, C., & Waters, L. B. F. M. 1995, *A&A*, 293, L25
- Varga, J., Hogerheijde, M., van Boekel, R., et al. 2021, *A&A*, 647, A56
- Verhamme, O., Kluska, J., Ferreira, J., et al. 2024, *A&A*, 684, A79
- Waelkens, C., Lamers, H. J. G. L. M., Waters, L. B. F. M., et al. 1991a, *A&A*, 242, 433
- Waelkens, C., Van Winckel, H., Bogaert, E., & Trams, N. R. 1991b, *A&A*, 251, 495
- Wang, Z. & Wu, L. 2023, *arXiv e-prints*, arXiv:2305.08404
- Weigelt, G., Hofmann, K. H., Schertl, D., et al. 2016, *A&A*, 594, A106
- Young, A. K., Stevenson, S., Nixon, C. J., & Rice, K. 2023, *MNRAS*, 525, 2616

Appendix A: Individual target descriptions

Below, we provide a more extensive discussion of our selected targets in the context of the existing literature, focusing on known properties and previous studies which provide insights on the structure and morphological complexity of the circumbinary disc.

A.1. AI Sco

AI Sco's primary is non- to weakly-depleted, as marked by its low zinc over titanium abundance of $[Zn/Ti] \sim 0.3$ dex (Giridhar et al. 2005). It is an RV Tauri type pulsator, and clearly shows the 'RVb' phenomenon (Kiss et al. 2007). This binary-associated effect describes a long-term modulation of photometric brightness superimposed on the shorter period variations caused by RV Tauri pulsations. The modulation periods typically match with spectroscopically derived orbital periods, and the primary star is often faintest and reddest at inferior conjunction. This supports the usual interpretation that the effect is caused by variable extinction along the line-of-sight (LOS) to the primary as it grazes the inner rim of the dusty circumbinary disc (e.g. Kiss et al. 2007; Manick et al. 2017). Detection of the RVb phenomenon is hence thought to imply a high inclination for the circumbinary dust disc – though (Kluska et al. 2019) found that the RVb phenomenon can occur for moderately inclined systems. While originally coined for RV Tauri stars, the term 'RVb phenomenon' is broadly used for any post-AGB system showing a similar long-term brightness modulation, regardless of whether the object is an RV Tauri pulsator or not.

Kluska et al. (2019) performed geometric modelling on a PI-ONIER snapshot survey of disc-bearing post-AGB binaries using models of varying complexity. The most complex models include a binary star, an up to second order azimuthally modulated Gaussian inner disc rim and an over-resolved background flux. This resulted in a best-fit model for AI Sco with a strong secondary detection at a flux fraction of $f_{sec,0} = 24.7^{+6.5}_{-6.9} \%$ (defined at reference wavelength $\lambda_0 = 1.65 \mu\text{m}$), a weak background flux at $f_{bg,0} = 1.1 \pm 0.4 \%$ and an inner rim with diameter $\theta_{rim} = 4.6 \pm 0.2$ mas, inclination $i_{rim} = 47.3^{+2.3}_{-2.6} \circ$ and position angle $PA_{rim} = 179^{+3}_{-3} \circ$. An inclined circular inner rim appears as an ellipse due to its projection on the plane of the sky. For a symmetrically and passively irradiated smooth disc, the primary H band brightness enhancement of the inner rim lies along the long side of the ellipse, symmetric with respect to the projected minor axis, due to self-absorption of the near side's emission (e.g. Hofmann et al. 2022). The main brightness enhancement of AI Sco's inner rim in the Kluska et al. (2019) model instead lies along the short side of the projected rim, seemingly in phase with the binary position of the primary (see their Fig. C.1 for model images of the disc rims).

A.2. EN TrA

EN TrA's primary is mildly depleted at $[Zn/Ti] \sim 0.6$ dex (Van Winckel 1997). It is an RV Tau pulsator, but no firm detection of the RVb phenomenon has been established yet (Van Winckel et al. 2009). The best-fit model by Kluska et al. (2019) shows a significant contribution from the secondary $f_{sec,0} = 7.8^{+1.7}_{-1.2} \%$, a weak over-resolved background $f_{bg,0} = 2.5^{+0.9}_{-1.0} \%$, and an inner rim with diameter $\theta_{rim} = 7.7^{+1.7}_{-1.6}$ mas and orientation of $i_{rim} = 52.7^{+7.8}_{-9.1} \circ$ and $PA_{rim} = 13^{+9}_{-7} \circ$. A strong azimuthal bright-

ness enhancement of the model disc appears aligned with the long side of the projected ellipse, which is also in phase with the position of the primary.

A.3. HD 95767

HD 95767 has a non-depleted primary at $[Zn/Ti] \sim 0.0$ dex (Van Winckel 1997). Kiss et al. (2007) marked it as a low-amplitude semi-regular or multiply periodic variable and firmly detected the RVb phenomenon, implying a possibly high inclination for the circumbinary disc. Kluska et al. (2019) fitted a model with a strong secondary companion flux at $f_{sec,0} = 12.3^{+2.3}_{-1.2} \%$, a weak background at $f_{bg,0} = 1.1^{+0.8}_{-0.7} \%$, and, contrary to what is expected from the clear presence of the RVb phenomenon, a pole-on inner rim at a diameter of $\theta_{rim} = 6.8^{+0.4}_{-0.5}$ mas. The main brightness enhancement along the rim seemed in phase with the primary's position.

The polar orientation derived by Kluska et al. (2019) is likely an artefact from their extremely sparse (u, v) coverage, covering only the small AT baselines. Our imaging results instead find a significantly non-zero inclination (Table 3).

A.4. HD 108015

HD 108015's primary is non-depleted at $[Zn/Ti] \sim 0.1$ dex (Van Winckel 1997). It was marked as a low-amplitude semi-regular or multiply periodic variable without an RVb phenomenon by Kiss et al. (2007). The best-fit model of Kluska et al. (2019) shows no detection of the secondary, a significant background flux at $f_{bg,0} = 8.5 \pm 0.4 \%$ and an inner rim with diameter $\theta_{rim} = 6.7 \pm 0.1$ mas and a low-inclination orientation of $i_{rim} = 12.9^{+4.7}_{-5.9} \circ$ and $PA_{rim} = 40^{+16}_{-19} \circ$. The main brightness enhancement along the rim is out of phase with the primary's position relative to the rim centre (with the primary's projected position likely being mostly a projection effect; see Sect. 5.3.4), and is instead shifted counter-clockwise. Geometric modelling of snapshot VLTI/MATISSE data by Corporaal et al. (2023a) using a model consisting of the primary and a power-law surface brightness disc (and modelling only the $V2$ data) resulted in a much smaller inner rim disc diameter of $\theta_{rim} = 3.4 \pm 0.6/3.6 \pm 0.2$ mas in L/N band respectively. The fitted orientation of the disc was $i_{rim} = 35 \pm 11/32 \pm 2 \circ$ and $PA_{rim} = 45 \pm 13/15 \pm 2 \circ$, which seems inconsistent with the lower inclination found by Kluska et al. (2019).

These inconsistencies between geometric modelling studies are likely caused by their sparse (u, v) coverages, causing strong parameter degeneracies between the rim size, orientation, and azimuthal and radial extent of the emission (this is why the rim orientation is best fixed during geometric modelling if constraints from other sources are available, as in e.g. Setterholm et al. 2025). This is compounded by the use of qualitatively different disc radial intensity profiles (Gaussian profiles in Kluska et al. 2019 versus radial power laws in Corporaal et al. 2023a). Our imaging results (Table 3) are more consistent with the rim size found by Kluska et al. (2019), but also more consistent with the inclination found by Corporaal et al. (2023b). We note that this does not invalidate the findings of either study, as each was internally consistent in their geometric modelling approach, and their main results were based on general distributions of the fit-

ted parameters (and, in the case of [Corporaal et al. 2023b](#), the relative comparison between different SED categories).

A.5. HR 4049

HR 4049 is an extremely depleted system, hallmarked by its remarkably low metallicity $[\text{Fe}/\text{H}] \sim -4.8$ dex and high zinc over iron ratio $[\text{Zn}/\text{Fe}] \sim 3.5$ dex ([Van Winckel et al. 1995](#); [Oomen et al. 2019](#)). Photometric studies identified the primary as non-pulsating, but the RVb phenomenon was firmly detected ([Waelkens et al. 1991a](#); [Kiss et al. 2007](#)). [Kluska et al. \(2019\)](#) fitted a model with a fairly weak secondary flux fraction at $f_{\text{sec},0} = 2.5^{+1.1}_{-0.8}$ % and strong background contribution of $f_{\text{bg},0} = 17.0 \pm 0.7$ %. The fitter inner rim presented a diameter of $\theta_{\text{rim}} = 16.4 \pm 0.5$ mas and orientation $i_{\text{rim}} = 49.3^{+3.2}_{-3.3}$ and $\text{PA}_{\text{rim}} = 63^{+7}_{-6}$ °. While a secondary brightness enhancement was in phase with the primary position, the main brightness enhancement appeared on the opposite side along the major axis of the projected disc.

The surface of the outer disc regions was imaged in the SPHERE/IRDIS *H* band polarimetric imaging study of eight disc-bearing post-AGB binaries by [Andrych et al. \(2023\)](#). The outer discs in this study appear as a bright central ‘ring’, marked by a low intensity cavity in the centre. This cavity is an artefact of the image reduction, caused by the subtraction of the central unresolved polarised flux. The disc orientation derived from this ring was deemed unreliable, as it provides a low inclination ($i \sim 16.8^\circ$) incompatible with the robust detection of the RVb phenomenon and the results of [Kluska et al. \(2019\)](#) (as well as our imaging results; Table 3). The circumbinary disc otherwise showed no potential substructures on the scales probed by IRDIS.

A.6. IRAS 15469-5311

IRAS 15469-5311’s primary is strongly depleted with $[\text{Zn}/\text{Ti}] \sim 1.8$ dex ([Maas et al. 2005](#)). While the primary pulsates, the pulsation pattern seems rather erratic, and not consistent with a classical RV Tau variable ([Kiss et al. 2007](#)). No clear photometric detection of an RVb phenomenon has been published yet. The [Kluska et al. \(2019\)](#) PIONIER snapshot model fit consists of a binary star, a significant over-resolved background at $f_{\text{bg},0} = 12.8^{+0.5}_{-0.6}$ % and an inner rim with diameter $\theta_{\text{rim}} = 10.4 \pm 0.3$ mas and orientation $i_{\text{rim}} = 53.5^{+1.8}_{-2.2}$ and $\text{PA}_{\text{rim}} = 64^{+2}_{-2}$ °. The secondary detection was highly tentative, with a flux fraction of only $f_{\text{sec},0} = 0.1^{+0.1}_{-0.1}$ %. The primary brightness enhancement lies along the long side of the projected rim, and is not in phase with the primary’s position, consistent with the expected RT effects of a symmetrically illuminated, smooth inclined disc rim. The MATISSE snapshot modelling by [Corporaal et al. \(2023a\)](#) resulted in a disc with an orientation of $i_{\text{rim}} = 47 \pm 5^\circ$ and $\text{PA}_{\text{rim}} = 50 \pm 4^\circ$. The inner rim diameter was found to be much smaller than the [Kluska et al. \(2019\)](#) value, at $\theta_{\text{rim}} = 3.4 \pm 0.4$ mas. As for

HD 108015, this is most probably caused by sparse (u, v) coverages and the resulting strong parameter degeneracies.

The outer disc surface was polarimetrically imaged by [Andrych et al. \(2023\)](#), revealing a bright central ring at an orientation of $i_{\text{rim}} = 19.6^{+18}_{-16}$ and $\text{PA}_{\text{rim}} = 139^{+27}_{-30}$ °. This orientation differs from that of the disc inner rim found by [Kluska et al. \(2019\)](#) and [Corporaal et al. \(2023a\)](#), again possibly due to data reduction artefacts affecting the central ring. These SPHERE observations also showed a secondary ring-like substructure offset from the central ring (see their Fig. 5). Interpreting these as part of one continuous disc, [Andrych et al. \(2023\)](#) derived a disc scale height of ~ 190 AU at a separation of ~ 1100 AU.

A.7. IW Car

IW Car is strongly depleted at $[\text{Zn}/\text{Ti}] \sim 2.1$ dex ([Giridhar et al. 1994](#)). It is an RV Tau pulsator with a firmly detected RVb phenomenon ([Kiss & Bódi 2017](#)). [Kluska et al. \(2019\)](#) fitted an inner rim model with a binary $f_{\text{sec},0} = 3.5 \pm 0.1$ % and a significant over-resolved component at $f_{\text{bg},0} = 10.5 \pm 0.3$ %. The fitted inner rim had a large diameter of $\theta_{\text{rim}} = 23.0^{+0.7}_{-0.6}$ mas and was remarkably broad (Gaussian full-width-half-maximum (FWHM) equal to $0.71 \pm 0.02 \theta_{\text{rim}}$). The rim was oriented at $i_{\text{rim}} = 44.6^{+1.7}_{-1.8}$ and $\text{PA}_{\text{rim}} = 155 \pm 2^\circ$. [Corporaal et al. \(2023a\)](#) fitted a smaller inner rim using VLT/MATISSE at $\theta_{\text{rim}} = 4.4 \pm 0.4/4.8 \pm 0.2$ mas in *L/N* band respectively (likely probing the inner flux arcs we resolve in our imaging; Sect. 5.3.7), though the model generally fails to fit the large baseline data in the *L* band.

IW Car was included in the SPHERE/IRDIS study of [Andrych et al. \(2023\)](#), where the system clearly presented a bright arc to the east of the usual central ring, separated by a dark shadow (see their Fig. 5). This was interpreted as scattered light from the two sides of the disc, separated by the optically thick near-side mid-plane, leading to a disc scale height estimate of ~ 190 AU. The central ring orientation was found to be, $i_{\text{rim}} = 41.7^{+6.5}_{-7.7}$ and $\text{PA}_{\text{rim}} = 161^{+12}_{-10}$ °, though it could again be affected by reduction artefacts.

A.8. PS Gem

PS Gem, similar to HR 4049, shows an extremely low metallicity and depleted primary at $[\text{Fe}/\text{H}] \sim -4.5$ dex and $[\text{Zn}/\text{Ti}] \sim 3.0$ dex. While not a regular RV Tauri variable, it does show the RVb phenomenon ([Waelkens et al. 1991b](#); [Kipper 2013](#); [Rao & Giridhar 2014](#)). [Kluska et al. \(2019\)](#) fitted a binary model to their PIONIER data, with no contribution of any disc signal. In addition to a background flux at $f_{\text{bg},0} = 4.3^{+0.7}_{-0.8}$ %, the fitted secondary flux fraction was relatively weak at $f_{\text{sec},0} = 2.4^{+1.6}_{-0.3}$ %, and its position relative to the primary was very poorly constrained at $\Delta\alpha_{\text{sec}} = 3.3^{+32.5}_{-35.6}$ mas and $\Delta\delta_{\text{sec}} = 5.0^{+23.7}_{-21.6}$ mas. Indeed, we do not recover a significant secondary detection in this study. The lack of disc signal in [Kluska et al. \(2019\)](#) was likely caused due to PS Gem’s extremely poor (u, v) coverage (a single snapshot at short baselines), as well as the generally low flux contribution of the disc (as found in this work; e.g. Table 3).

Appendix B: Geometric model images and synthetic data reconstructions

Images of the final PMOIREED geometric disc models fitted to our targets (Table 2) are shown in Fig. B.1. These images show the underlying analytical intensity distributions used to initially model the inner disc rim in Sect. 4.2. We stress that the goal of these geometric models is not to fully reproduce the complex rim emission morphology or act as initial starting images for the image reconstructions, but to procure preliminary estimates for the SPARCO parameters as initial values for the BADS SPARCO optimisation routine (Sect. 4.3.2). As such, we have only included up to one order of azimuthal modulation for the

rim brightness profile, which can cause morphological model biases if the true underlying azimuthal brightness profiles have sharper features or are generally more complex (e.g. AI Sco’s model reaching only a poor goodness of fit at $\chi^2_v \sim 5$ and being biased in PA towards the primary; Sect. 5.3.1). Nevertheless, analysing the behaviour of reconstructions of these models under analogous circumstances to our INSPIRING datasets can help identify potential biases in the imaging procedure and rim parameter derivation.

B.1. Bias assessment through synthetic reconstructions

To assess potential biases in our imaging workflow (Sect. 4.3) which might affect the interpretation of the final images, we applied our ORGANIC workflow on synthetic $V2$ and $\phi3$ datasets derived from the PMOIREED geometric models. This includes BADS optimisation of the free SPARCO parameters ($f_{\text{prim},0}$, UD_{prim} , $f_{\text{sec},0}$ & d_{rim} ; starting from their values in Table 2). The synthetic datasets use the same (u, v) coverage and noise levels as the observations (Figs. 1 & E.1). The imaging parameters (SF, PS & FOV) were set to those used in Table 3.

We focus on assessing any potential biases in the image-derived rim parameters, as well as the position of morphological features such as azimuthal brightness enhancements. The rim parameters themselves, including θ_{rim} , i_{rim} and PA_{rim} , are chosen from Table 2 for the geometric models themselves, and are de-

rived from the reconstructions following the rim fitting routine described in Sect. 5.1. Radial brightness profiles were then calculated following Sect. 5.1. In addition, we also calculated the azimuthal brightness profiles by integrating the flux along radial rays from the rim centre, separated by 0.1° in on-sky position angle PA, within elliptical apertures following the rim orientation. We show the images reconstructed from the synthetic model datasets versus their ground truth counterparts in Fig. B.2. The corresponding brightness profiles are given in Fig. B.2. The image-derived rim parameters are given in Table B.1.

We find the following potential biases for the rim parameters (we discuss those that are of $\geq 2\sigma$ significance) and rim morphology of note for each of our targets:

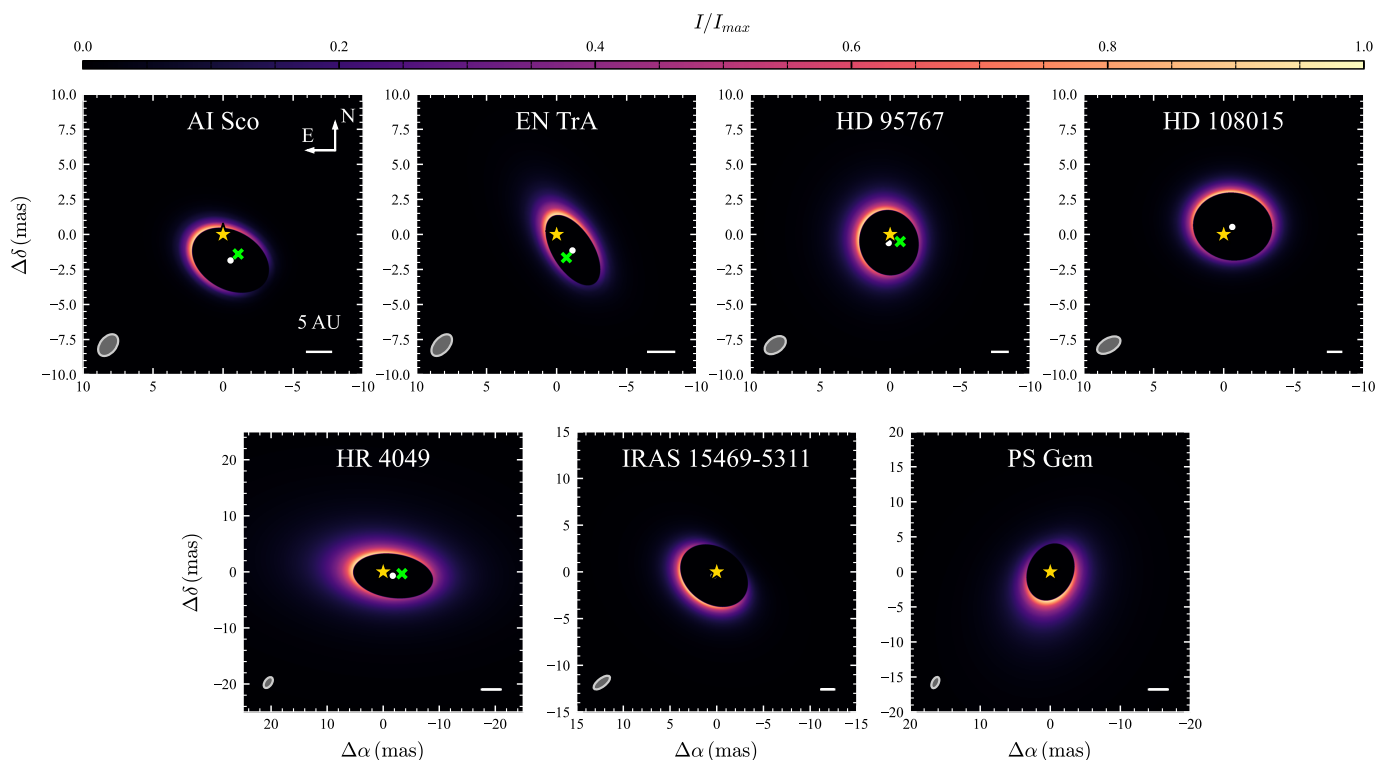


Fig. B.1: Analytical PMOIREED model disc images (Table 2). All other symbols are analogous to those in Figs. 3 & 4.

Table B.1: SPARCO and image-derived rim parameters of the synthetic PMOIREd data reconstructions.

Target	$f_{\text{prim},0}$ (%)	UD_{prim} (mas)	$f_{\text{sec},0}$ (%)	d_{rim}	θ_{rim} (mas)	i_{rim} ($^{\circ}$)	PA_{rim} ($^{\circ}$)	$\Delta\alpha_{\text{rim}}$ (mas)	$\Delta\delta_{\text{rim}}$ (mas)	r_{hl} (mas)
AI Sco	67.1	–	5.49	0.64	$5.8^{+0.5}_{-0.4}$	42^{+6}_{-8}	56^{+6}_{-5}	$-0.35^{+0.11}_{-0.14}$	$-1.72^{+0.17}_{-0.20}$	$3.23^{+0.12}_{-0.12}$
EN TrA	72.1	–	4.99	0.30	$6.50^{+0.20}_{-0.16}$	52^{+2}_{-2}	30^{+4}_{-5}	$-1.04^{+0.04}_{-0.04}$	$-0.94^{+0.11}_{-0.13}$	$3.86^{+0.13}_{-0.13}$
HD 95767	47.4	–	22.08	1.91	$5.66^{+0.06}_{-0.05}$	20^{+3}_{-3}	21^{+3}_{-6}	$0.02^{+0.03}_{-0.03}$	$-0.61^{+0.03}_{-0.03}$	$3.43^{+0.13}_{-0.13}$
HD 108015	56.7	–	–	1.29	$6.31^{+0.06}_{-0.06}$	$26.3^{+1.6}_{-0.9}$	$77.3^{+3.2}_{-1.7}$	$-0.57^{+0.03}_{-0.03}$	$0.47^{+0.04}_{-0.04}$	$3.62^{+0.16}_{-0.16}$
HR 4049	65.5	0.74	0.30	2.40	$16.6^{+0.7}_{-0.7}$	48^{+3}_{-3}	85^{+5}_{-5}	$-1.1^{+0.3}_{-0.3}$	$-0.78^{+0.17}_{-0.17}$	16^{+2}_{-2}
IRAS 15469-5311	52.7	–	–	2.04	$8.76^{+0.09}_{-0.08}$	$34.8^{+1.1}_{-0.6}$	52^{+5}_{-4}	$0.38^{+0.06}_{-0.06}$	$-0.30^{+0.05}_{-0.05}$	$5.30^{+0.29}_{-0.14}$
PS Gem	89.1	0.44	–	0.67	$10.5^{+0.9}_{-0.8}$	36^{+8}_{-8}	151^{+11}_{-8}	$-0.1^{+0.3}_{-0.3}$	$0.0^{+0.5}_{-0.4}$	$9.8^{+0.9}_{-1.1}$

AI Sco: comparing the reconstruction with the model ground truth in Fig. B.2, we note that the reconstructed disc flux close to the position of the primary star is biased in position by about ~ 1 mas southwards from where it is supposed to be, and seems systematically fainter. This also causes the reconstructed radial brightness profile to be slightly shifted and extended inwards, and the peak of the azimuthal brightness profile to be slightly shifted (by $\sim 20^{\circ}$ in PA) from its fiducial position (Fig. B.3). This artefact is likely caused by the close approach of the primary to the rim, and the sparsity of north- and north-west oriented long-baseline observations (Fig. 1). This causes the reconstruction routine to be unable to fully distinguish between flux from the primary’s position and flux from the nearest part of the rim. This artefact can also be seen in both our final ORGANIC reconstructions (Fig. 3) and the additional SQUEEZE reconstructions (Fig. D.1). Nevertheless, this does not affect our main imaging results significantly: the brightness enhancement is heavily shifted towards the rim’s projected major axis (Sect. 5.3.1). All rim parameters are properly retrieved without clear biases (i.e. consistency within 2σ between Tables B.1 & 2).

EN TrA: comparing Tables B.1 & 2, we note a bias of $0.87^{+0.20}_{-0.16}$ mas in θ_{rim} and of -7^{+2}_{-2} in i_{rim} . These are caused by the limited resolution of the interferometer, which smears out the infinitely sharp model rim, where the model intensity suddenly jumps from zero before decaying with a power law. This pulls the intensity peak slightly backward and blurs the sharp ellipticity of the model rim. This induces a systematic positive bias for θ_{rim} , and a negative bias for i_{rim} . These biases are a common occurrence for our targets, as seen from the discussion of the other targets below. There is also a slight potential bias in $\Delta\alpha_{\text{rim}}$ of $0.09^{+0.04}_{-0.04}$ mas. Nevertheless, these findings do not significantly affect our main results: the brightness enhancement is positioned along the rim’s projected major axis (Sect. 5.3.2). Aside from some mild flux leakage into the central cavity, the brightness profiles are generally well-recovered (Fig. B.3).

HD 95767: we note a bias of $0.99^{+0.06}_{-0.05}$ mas in θ_{rim} and of -6^{+3}_{-3} in i_{rim} (Tables B.1 & 3). There is also a slight potential bias in $\Delta\alpha_{\text{rim}}$ of $-0.09^{+0.03}_{-0.03}$ mas. These do not affect the main results discussed in Sect. 5.3.3: the final image is highly sensitive to (u, v) coverage specifics and is hence not included in the discussion on potential substructures. The radial and azimuthal profile are well-recovered (Fig. B.3).

HD 108015: we note a bias of $0.68^{+0.06}_{-0.06}$ mas in θ_{rim} and of $-4.9^{+1.6}_{-0.9}$ in i_{rim} (Tables B.1 & 3). There is also a potential bias in PA_{rim} of $-5.2^{+3.2}_{-1.6}$. These do not affect the main results presented in Sect. 5.3.2: the brightness enhancement is significantly shifted towards the rim’s projected major axis. The radial and azimuthal brightness profiles are well-recovered (Fig. B.3).

HR 4049: we find potential biases of $2.3^{+0.7}_{-0.7}$ mas in θ_{rim} and -9^{+3}_{-3} in i_{rim} (Tables B.1 & 3). These do not significantly affect the main results presented in Sect. 5.3.5: the brightness enhancement is significantly shifted towards the rim’s projected major axis. Aside from a minor amount of flux leakage in the central cavity drawing the radial brightness profile slightly inward, the radial and azimuthal brightness profiles are recovered (Fig. B.3).

IRAS 15469-5311: we find potential biases of $0.96^{+0.09}_{-0.08}$ mas in θ_{rim} and $-5.4^{+1.1}_{-0.6}$ in i_{rim} (Tables B.1 & 3). These do not significantly affect the main results presented in Sect. 5.3.6: the brightness profile is mostly symmetric around rim’s projected minor axis, with no other robust brightness enhancements detected. The radial and azimuthal brightness profiles are recovered (Fig. B.3).

PS Gem: we find a potential bias of $2.1^{+0.9}_{-0.8}$ mas in θ_{rim} (Tables B.1 & 3). The reconstruction shows some pixelation and dirty beam artefacts, especially in faint flux regions (Fig. B.2), causing a bump in the tail of the reconstructed radial brightness profile (Fig. B.3). The trend of the radial and azimuthal profiles are otherwise both well-recovered (Fig. B.2). This does not significantly affect the main results presented in Sect. 5.3.8: PS Gem’s image in Fig. 4 is most likely marred by the strong flux leakage from the primary, and it is thus excluded from the discussion on potential substructures.

In general, the only bias relative to the geometrical models that seems common to all systems is a positive bias of ~ 1 – 2 mas is the rim diameter and a negative bias of several degrees in inclination (though always $\lesssim 10^{\circ}$ in magnitude). This is a natural result of the infinitely sharp rim assumed in the geometric models, which when viewed at the interferometer’s angular resolution results in a slightly radially outwards shifted peak flux. The rim fitting routine targets this peak flux to derive θ_{rim} . It also slightly blurs the apparent ellipticity of the rim, lowering the apparent inclination. It should be noted that the biases are only of concern if the true inner rims are indeed sharp and wall-like. At least for inner rims set by sublimation physics, there is reason to suspect that this is not the case (see the discussion at the end of Sect. 6.1.1).

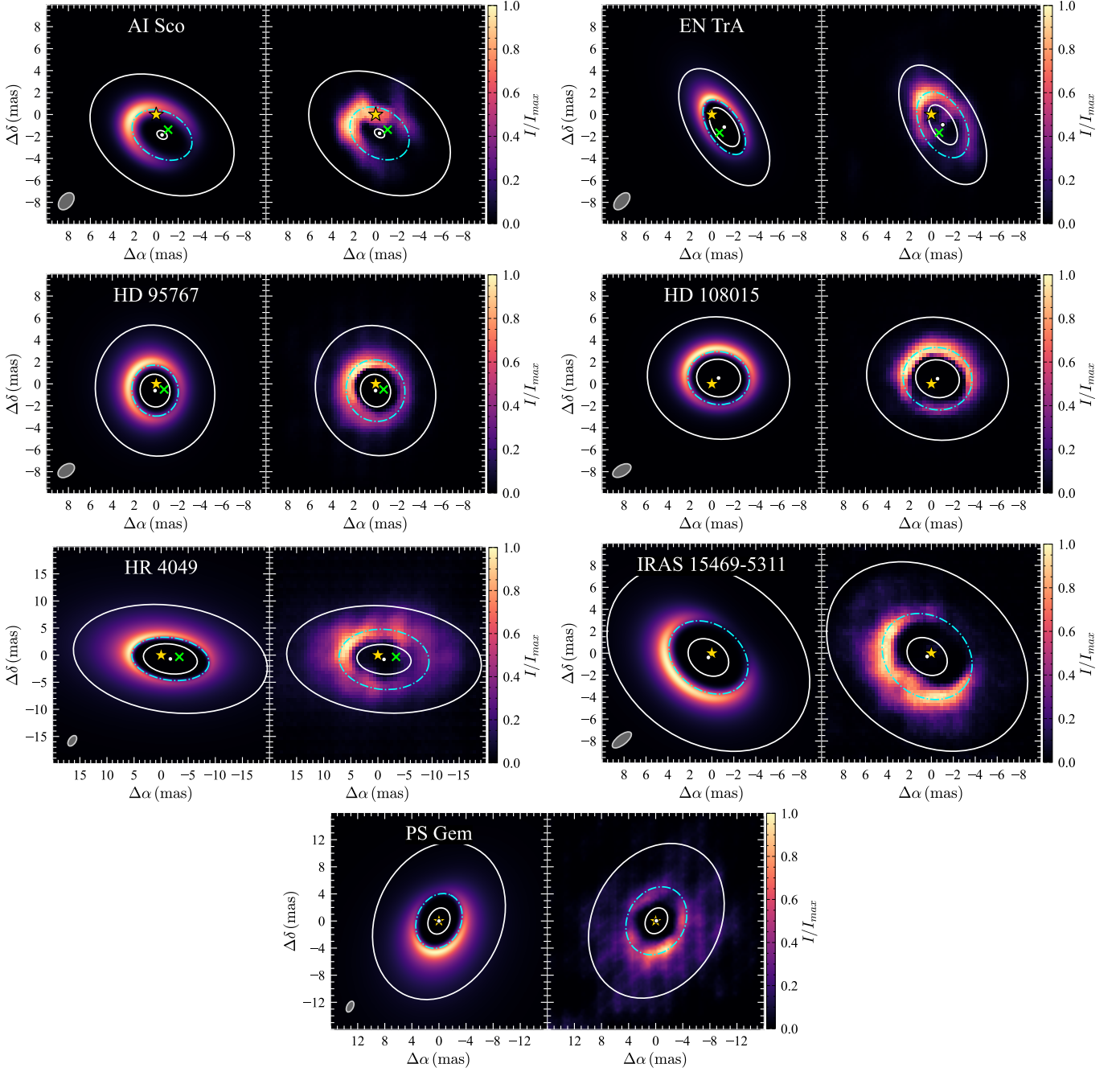


Fig. B.2: PMOIRED images of Fig. B.1, convolved by a Gaussian to match the imaging resolution (left-hand images), versus their reconstruction from synthetic datasets (right-hand images). White solid lines indicate the elliptical aperture following the rim orientation used to calculate the azimuthal brightness profiles. The rim orientation is taken from Table 2 for the PMOIRED images, and from Table B.1 (i.e. derived from the images following Sect. 5.1) for their reconstructions. These rims are displayed in dot-dashed cyan. All other symbols analogous to Figs. 3 & 4.

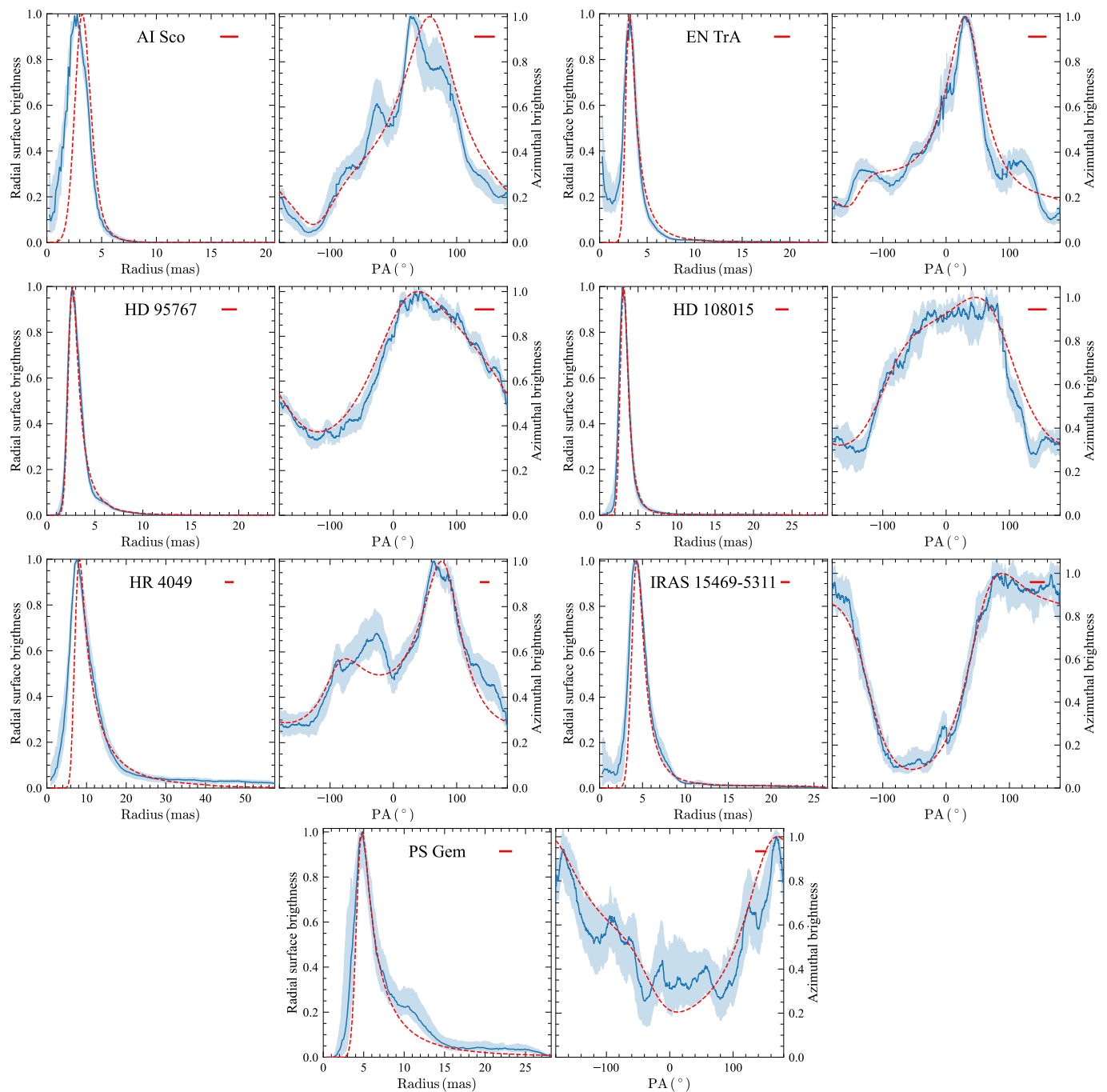


Fig. B.3: Peak-normalized radial and azimuthal brightness profiles of the convolved model images (red dashed) and synthetic reconstructions (blue with 1σ contours) in Fig. B.2. Red bars indicate the size of the azimuthally averaged interferometric beam (for the radial profiles) and the PA it subtends at the reconstruction's rim (for the azimuthal profiles).

Appendix C: Effect of regularisation weight on ORGANIC reconstructions

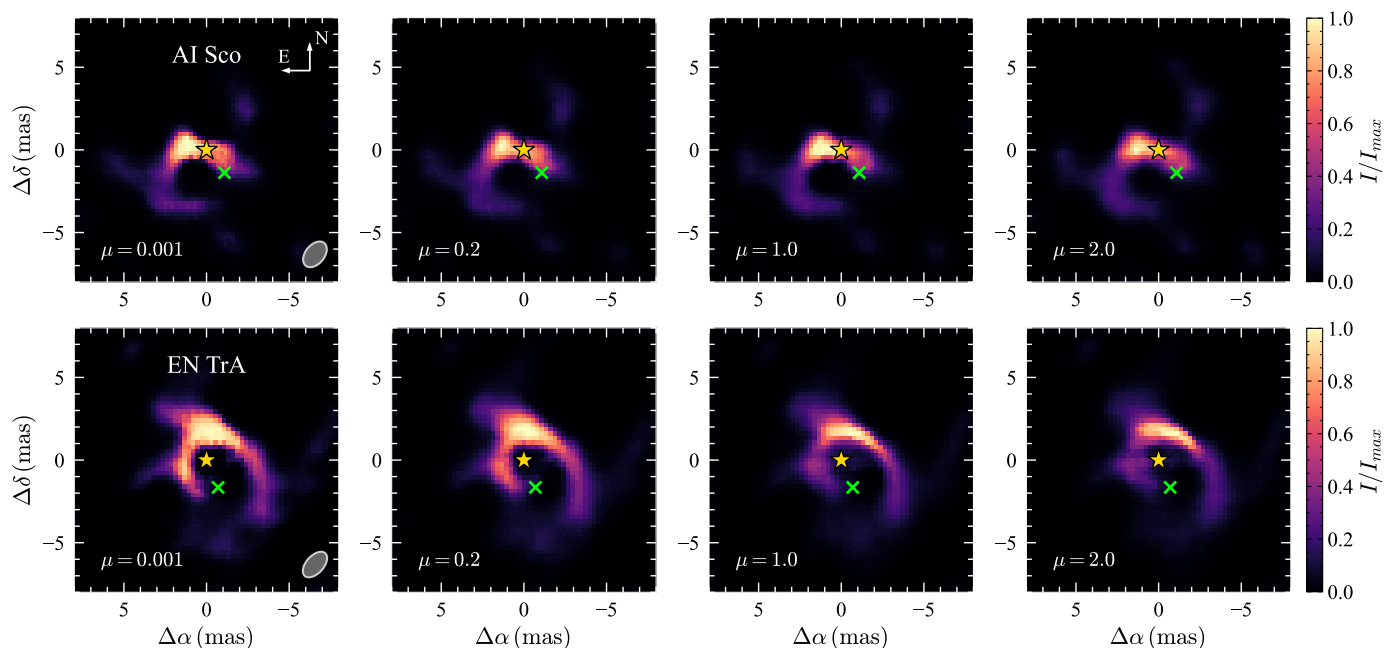


Fig. C.1: Illustration of the effect of different values for the regularisation weight μ . The interferometric beam size is given in the lower-right corner. All other symbols are analogous to Fig. 3.

In this appendix, we investigate the effect of the regularisation weight μ on the ORGANIC images.

The total reconstruction loss in ORGANIC utilises the score output of the GAN discriminator evaluated on the generated image, \hat{s}_{img} , as a regularisation term (via $\mathcal{L}_{\text{reg}} = -\ln \hat{s}_{\text{img}}$). Its aim is to make the imaged rims look more like the RT model training data. In this section, however, we show that most of the regulatory properties of ORGANIC are not caused by the numerical weight of \mathcal{L}_{reg} in the total reconstruction loss (Eq. 4), but are instead inherent to the CNN architecture itself, as well as the initial training of the generator’s convolutional kernel weights.

Fig. C.1 shows example ORGANIC images for AI Sco and EN TrA at various values of the regularisation weight μ (using the same parameters as in Table 3). Higher μ generally leads to slightly less pixelation, radially sharper rims and more sharply defined azimuthal brightness modulations (though over-regularisation tends to occur for $\mu \gtrsim 1$, making the rim too sharp, as seen for EN TrA). Nevertheless, the recovered structures are highly similar, especially on the scale of the interferometric beam. This holds even for $\mu = 0.001$, which renders the numerical weight of \mathcal{L}_{reg} negligible. At very low μ values, most differences are likely stochastic in nature, induced by the random initialisations of the latent noise vector and the Monte Carlo dropout layers in ORGANIC (Claes et al. 2020). ORGANIC clearly possesses an implicit regularisation floor.

A similar implicit regularisation was noticed and utilised by the PIRATES⁹ image reconstruction framework of Lilley et al. (2026). The authors presented a CNN which is applied directly on polarimetric masking interferometry data from the VAMPIRES instrument (Lucas et al. 2024). In a first initial training

step, the convolutional kernel weights of the network are trained to map from a set of VAMPIRES observables to a cube of images in Stokes (I, Q, U) space. The training set for this step consists of sets of Stokes scattered light image cubes for various dusty geometries and their corresponding VAMPIRES observables, modelled using the MCFOST¹⁰ RT code (Pinte et al. 2006, 2009). This forces the CNN kernels to learn the scattering-induced, physically meaningful spatio-polarimetric relationships between images of different Stokes components. At reconstruction time, when faced with an arbitrary set of VAMPIRES observables, the initially trained CNN directly maps to a corresponding (I, Q, U) image cube. In a second step, this resulting initial image cube is refined by an iterative fitting routine. The initially trained kernel weights of the CNN are trained further in order to match the predicted interferometric observables, calculated from the CNN-generated image, to those actually observed. The generated image cube at the end of this procedure is taken as the final reconstruction. This results in well-regularised (I, Q, U) images which provide a good match to the data, but also retain the scattering-induced connections between different Stokes components.

The iterative fitting routine in PIRATES is highly similar to ORGANIC’s reconstruction algorithm. The ORGANIC reconstruction routine also updates the initially trained generator kernel weights in order to make the generated image match a set of interferometric data. The main difference between the two is that PIRATES acts directly on VAMPIRES observables, while ORGANIC acts on a latent noise space (allowing for reconstruction at arbitrary (u, v) coverage, but inducing an additional source of uncertainty; Sect. 4.3.1). At no point does PIRATES include an explicit \mathcal{L}_{reg} term in its reconstruction. Instead, it relies fully on

⁹ <https://github.com/SAIL-Labs/PIRATES>

¹⁰ <https://github.com/cpinte/mcfost>

the general inductive bias imparted by CNN architectures (such as locality and weight-sharing, e.g. Wang & Wu 2023; Ulyanov et al. 2020) – a property shared by other types architectures, such as neural fields, when applied to similar ill-posed inverse reconstruction problems (e.g. Levis et al. 2024) – as well as the initial training. The latter pre-emptively forces the weights into a subspace which generates images similar to the training data. Together with the limited effect of μ in ORGANIC, this shows that most of ORGANIC’s regulatory properties share similar origins. They are implicitly imposed by the generator’s CNN architecture and the initial training phase, not by the numerical weight of \mathcal{L}_{reg} in the total loss.

The standard GAN architecture of ORGANIC precludes us from determining μ through the conventional L-curve method (e.g. Renard et al. 2011; see Appendix D for a description). This is due to the use of the discriminator score output in \mathcal{L}_{reg} . The discriminator score estimates the Jensen-Shannon divergence between the image during reconstruction and the RT training set (Goodfellow et al. 2014). This is a good distance measure during the initial phases of the image reconstruction, and does

Appendix D: SQUEEZE reconstructions

As further validation of our ORGANIC image reconstruction procedure (Sect. 4.3), we additionally performed image reconstructions on our targets using the SQUEEZE¹¹ package (Baron et al. 2010). SQUEEZE uses a more classical minimisation engine and set of regularisations. We used SQUEEZE’s implementation of SPARCO for a binary star (called `modelcode_binary_bwsmearing` internally). We then performed reconstructions using the same imaging and SPARCO parameters as in Table 3. SQUEEZE uses an annealed MCMC routine with Metropolis-Hastings steps in order to minimise the loss, and includes various classical regularisation functions. The annealing scheme is intended to encourage convergence to the global minimum compared to more prevalent gradient-descent-based methods. Starting from different random images and using total variation (TV) regularisation – which tends to produce piece-wise flat images (Thiébaud & Young 2017) – we ran 5 parallel MCMC chains for 2000 steps. Annealing generally converged after ~ 100 . The mean of the final 200 images of each chain was then taken as the final image. The regularisation weight μ was set through the L-curve method (e.g. Renard et al. 2011). This method consists of performing reconstructions for different values of μ , with the resulting plot of $\mathcal{L}_{\text{data}}$ versus \mathcal{L}_{reg} showing an L-like curve. This curve represents a transition regime between dominance of one loss term over the other. The optimal μ value is chosen in the knee of this curve. The resulting SQUEEZE images are shown in Fig. D.1.

To provide a more quantitative assessment of the similarity between the ORGANIC and SQUEEZE reconstructions, we also provide radial (following Sect. 5.1) and azimuthal (following Sect. B.1) brightness profiles. These are calculated using elliptical apertures following the rim orientations given in Table 3. The profiles are displayed in Fig. D.2. We find the following for each of our targets:

AI Sco: Both methods agree on the general shape of the radial and azimuthal profile. The SQUEEZE image’s TV regularisation does tend to produce a slightly broader radial profile and less pronounced azimuthal brightness depression of the disc flux close to the primary’s position (though this depression is likely

guide towards more regularised final images (as seen from Fig. C.1). However, as the reconstruction progresses and the similarity between the image and training set decrease, the Jensen-Shannon divergence saturates to similar values and becomes uninformative as a measure (Arjovsky & Bottou 2017). This can be addressed in future ORGANIC designs by using a Wasserstein GAN, where the discriminator instead produces an actively calculated estimate of the Wasserstein distance (Arjovsky et al. 2017). When used as the regularisation loss \mathcal{L}_{reg} , this Wasserstein estimate would remain an informative measure between the reconstructed image and the RT training set at all times. Since this would require an architectural overhaul of ORGANIC, this is currently beyond the scope of this work.

We performed initial investigations of the image morphologies for all targets under varying μ within a reasonable range ($\mu = 0.1$ – 2). The main recovered features do not vary significantly under varying μ . As it generally provided a good balance between suppression of noisy features and avoiding over-regularisation for our PIONIER datasets, we fixed $\mu = 0.2$ for the final ORGANIC reconstructions in this article (Figs. 3 & 4).

partially an artefact of the (u, v) coverage; Sect. B.1). This is due to the tendency of TV to prefer broad, piece-wise flux plateaus and heavy punishment of flux gradients between pixels within those plateaus (e.g. Rudin et al. 1992).

EN TrA: Both methods agree well on the azimuthal profile. As for AI Sco, the TV regularisation of the SQUEEZE image tends to produce a slightly broader radial profile.

HD 95767: Both methods agree well on the radial profile. The ORGANIC azimuthal profile, while sharing its main features with the SQUEEZE profile, is generally choppier, and unphysical broadening of the rim causes a secondary azimuthal brightness spike at PA $\sim 120^\circ$. This choppy nature is likely caused by dirty beam artefacts (see Sect. F.2). The TV regularisation more heavily punishes these features, resulting in a smoother azimuthal profile.

HD 108015: Both methods agree well on both the radial and azimuthal profile. The exact azimuthal position of the brightness enhancement of the rim differs by $\sim 10^\circ$ in PA, and the enhancement is slightly broader for the ORGANIC image. Nevertheless, this does not significantly affect the main results presented in Sect. 5.3.2: the brightness enhancement is significantly shifted towards the rim’s projected major axis.

IRAS 15469-5311: Both methods agree well on the radial profile. The azimuthal profiles also match in main features, indicating a rim mostly symmetric along its projected minor axis with no other strong brightness enhancements of note. The TV regularisation of the SQUEEZE image does discourage narrow flux features surrounded by pixels of little flux, resulting in a deeper flux depression along the darkest part of the rim.

IW Car: Both methods agree on the general features of the radial and azimuthal profiles for both the inner and outer arcs. However, there are mismatches in the specifics of the azimuthal profiles, such as the brightness of the inner arcs’ southeastern sector. This indicates that the specifics of the azimuthal profiles for IW Car are not entirely well-constrained, and should be treated with caution. This nevertheless does not affect the main results presented in Sect. 5.3.7: both inner arcs and a large outer arc are retrieved in the morphology.

¹¹ <https://github.com/fabienbaron/squeeze>

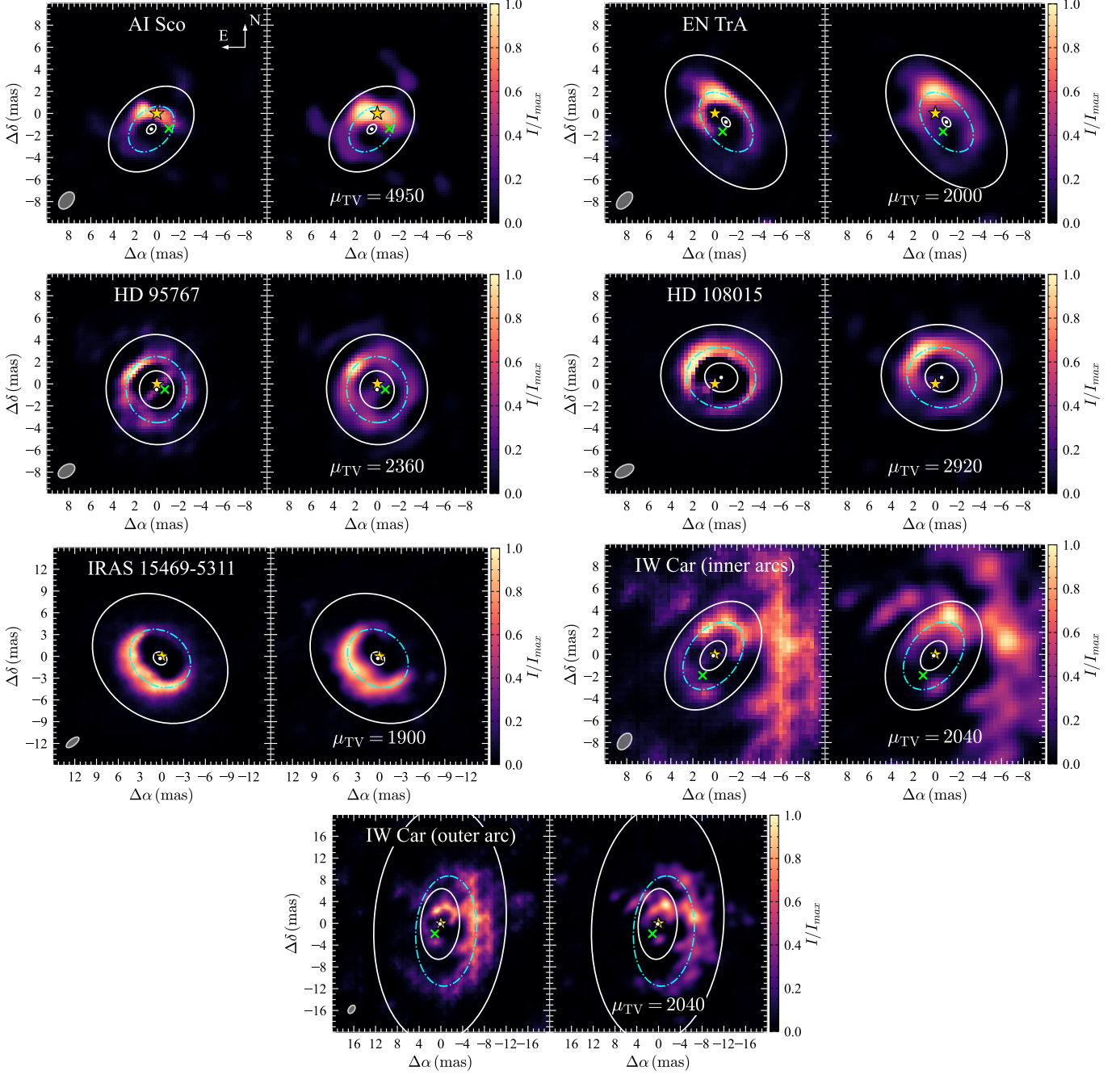


Fig. D.1: Comparison between our final ORGanic reconstructions (left-hand images; Figs. 3 & 4) and the alternative SQUEEZE reconstructions (right-hand images). The TV regularisation weight μ_{TV} is displayed for each SQUEEZE reconstruction. White solid lines indicate the elliptical aperture used to calculate the azimuthal brightness profiles. In dot-dashed cyan, we display the rim fits derived from the ORGanic images (Table 3), whose orientation is used to define the azimuthal profile aperture. Note that for IW Car’s outer arc, the elliptical aperture is centred on $(\Delta\alpha_{rim}, \Delta\delta_{rim})$ of the rim fit to the inner arcs. This is so the inner arcs can be properly masked out when calculating the outer arc’s azimuthal profile. The PA of the azimuthal profile and the centre of the radial profile are thus also defined from this point. All other symbols analogous to Fig. 3.

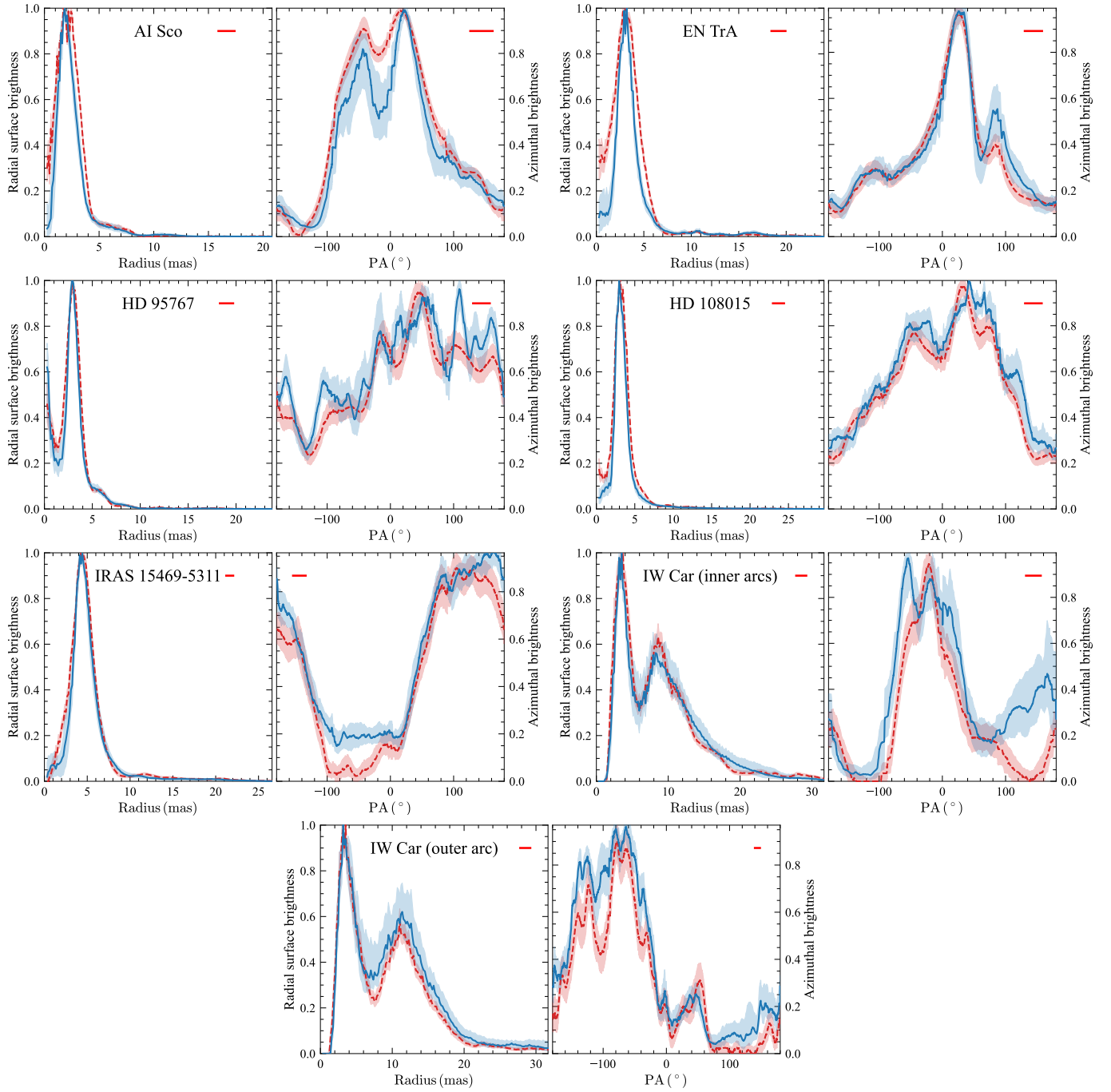
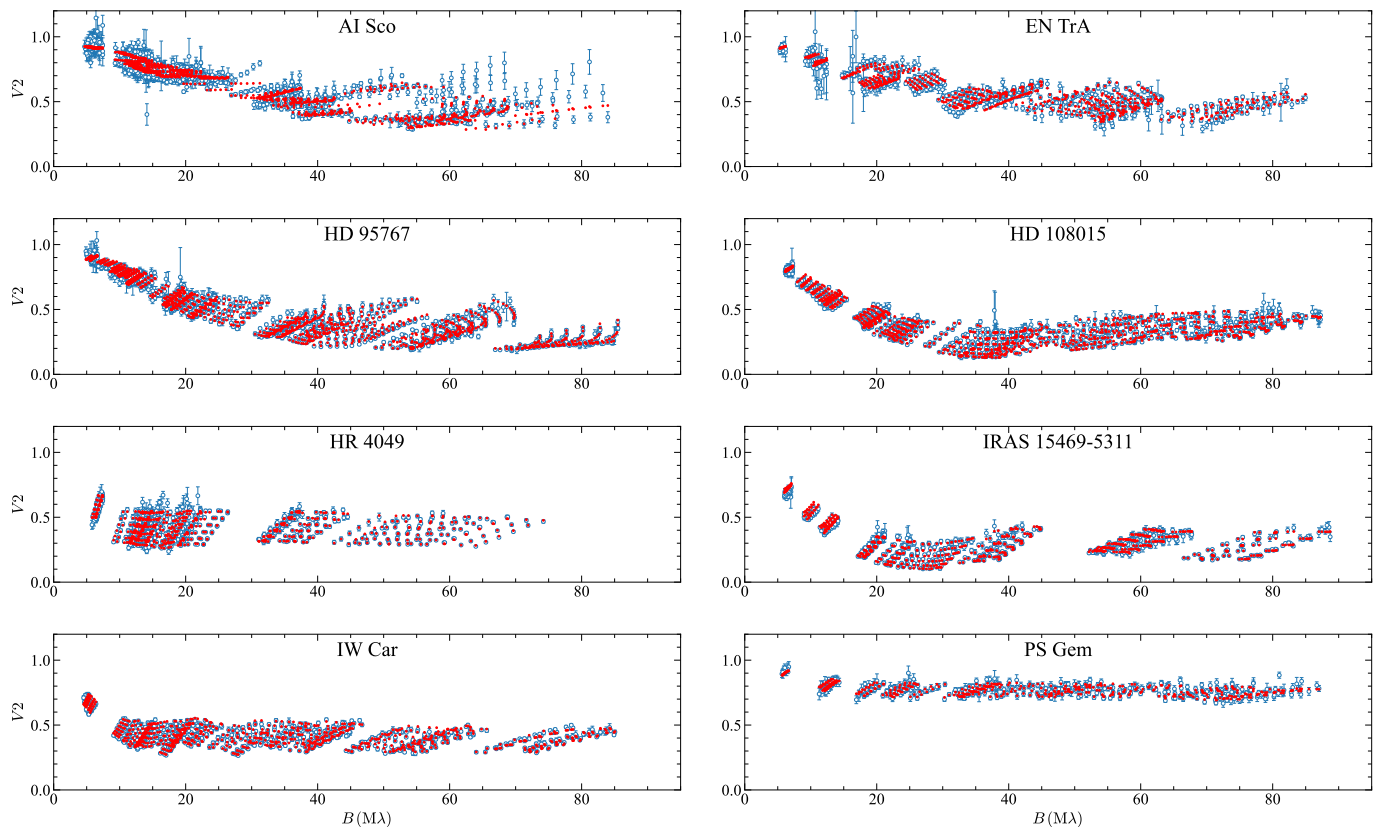


Fig. D.2: Peak-normalized radial and azimuthal brightness profiles of the ORGanic (solid blue) and SQUEEZE (dashed red) image reconstructions displayed in Fig. D.1. Both types of images are displayed with their 1 σ significance contours. Red bars indicate the size of the azimuthally averaged interferometric beam (for the radial profiles) and the PA it subtends at the reconstruction's rim (for the azimuthal profiles).

Appendix E: Selected data

The (u, v) coverages and observables of the selected PIONIER observations are shown in Figs. 1 & E.1. Corresponding observation logs are available online on [Zenodo](#).

Squared visibilities



Closure phases

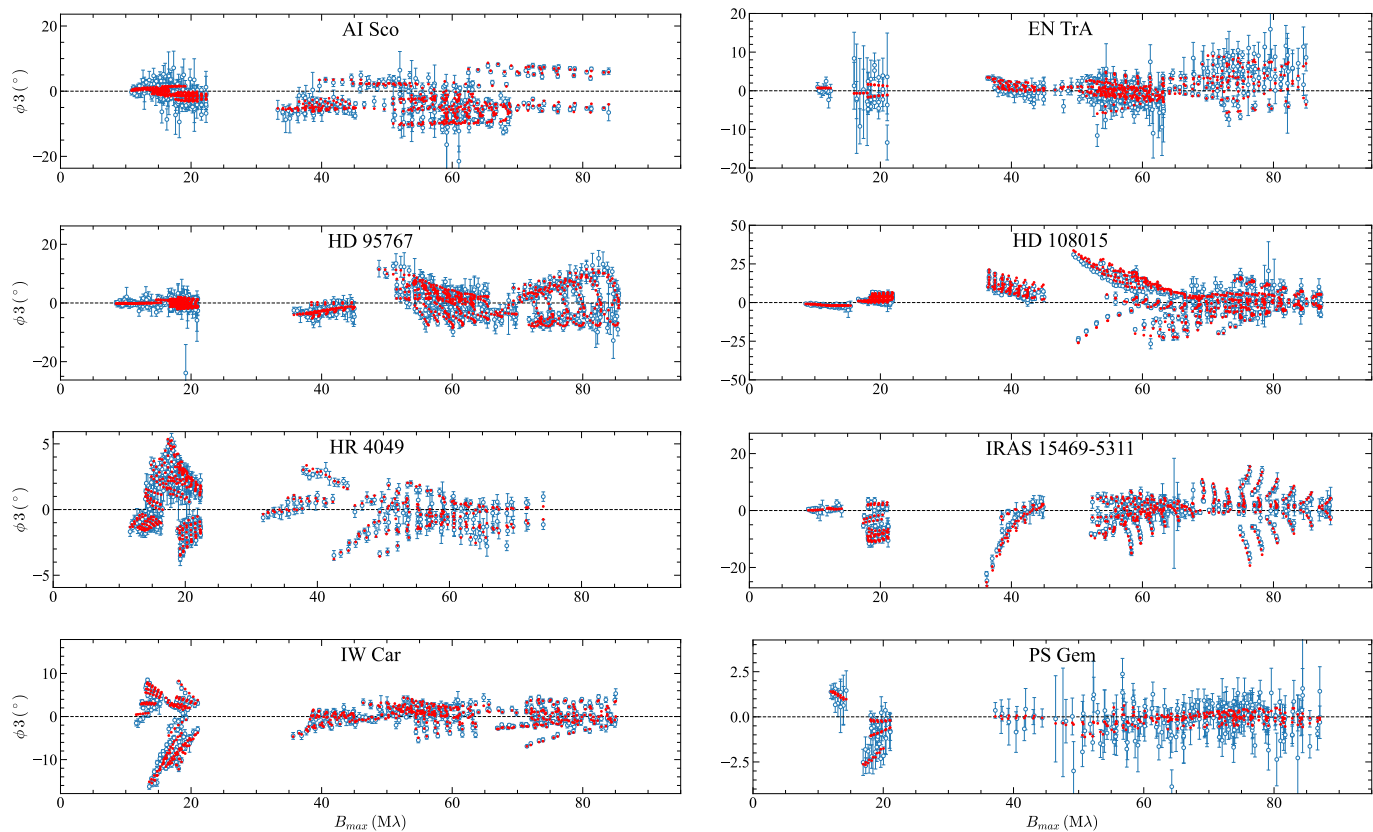


Fig. E.1: Selected V_2 and ϕ_3 data from the INSPIRING PIONIER observations of our targets, shown in blue. For comparison, the observables synthesised from the final SPARCO+ORGANIC image reconstructions (Figs. 3 & 4) are overlaid as red dots.

Appendix F: Image robustness against (u, v) coverage artefacts

In this appendix, we assess the robustness of our ORGANIC image reconstructions (Figs. 3 & 4) against any dirty beam artefacts potentially induced by the sparse (u, v) coverage of our observations. Such artefacts are often characteristic of optical interfer-

ometry due to the low number of telescopes used, and if left unidentified, can significantly bias the interpretation of recovered image features.

F.1. Dirty beams

The sparse (u, v) coverage in optical interferometry can be the cause of non-physical artefacts in the reconstructed images, which have no basis in the actual object's intensity distribution. These artefacts are caused by secondary lobes in the interferometric point spread function, also called the dirty beam. The dirty beam is calculated using the inverse direct Fourier transform, assuming a point source frequency response (i.e. a visibility of unity) at the sampled (u, v) points and zero visibility elsewhere. In Fig. F.1, we show the dirty beams corresponding to our target's (u, v) coverages (Fig. 1). The centre of the dirty beam consists of an elliptical Gaussian-like peak called the pri-

mary beam. The centre of this peak is called the interferometric beam size – with a short side is of size $\sim \lambda_{\min}/(2B_{\max})$, with λ_{\min} the shortest wavelength and B_{\max} the longest baseline – and defines the formal resolution element of the observations. Further away from the primary beam, one can see multiple other features (even negative flux features, which can cause subtraction effects), called secondary lobes, which are the cause of reconstruction artefacts. In the following, we will apply a test which can help identify such artefacts in our final ORGANIC reconstructions.

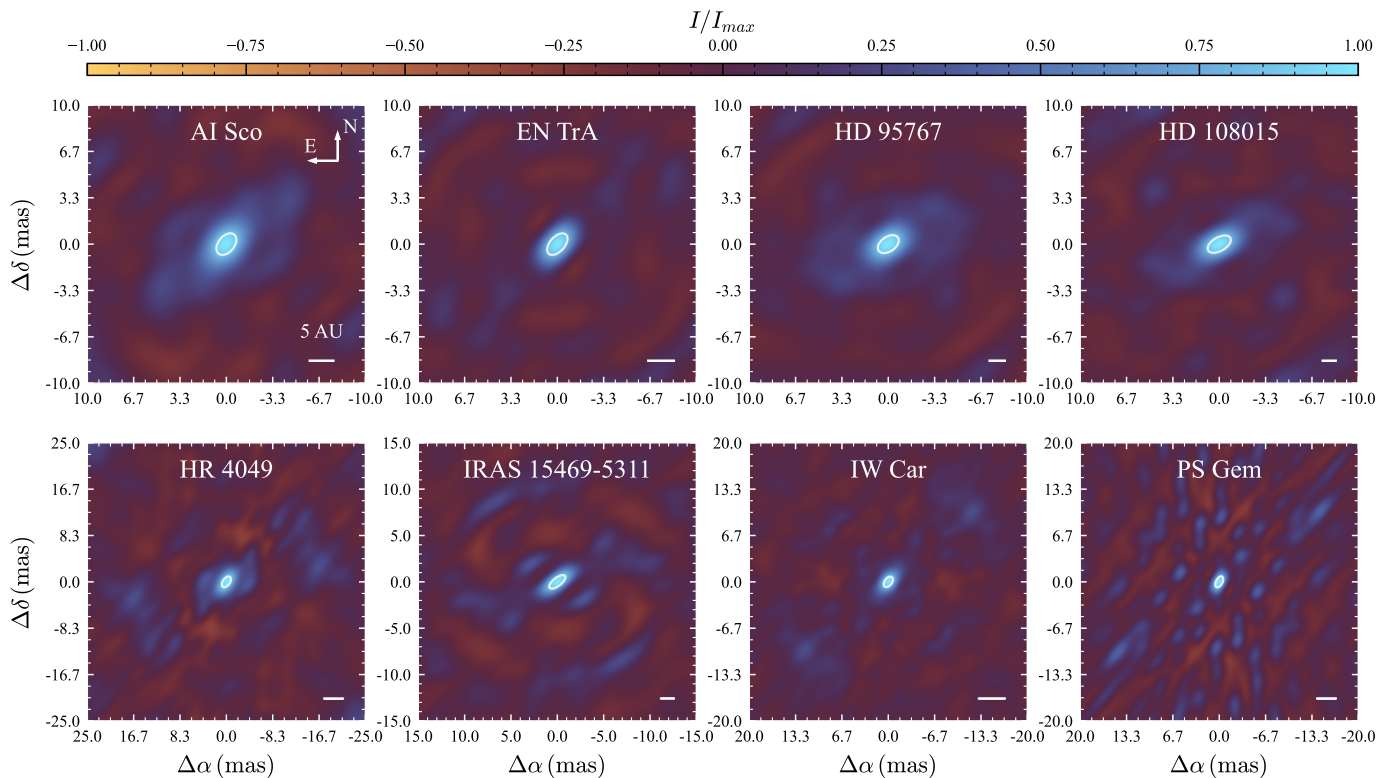


Fig. F.1: Dirty beams of the observations. Calculated using the sampled (u, v) coverages in Fig. 1. Central ellipses denote the interferometric beam (short side of size $\sim \lambda_{\min}/(2B_{\max})$).

F.2. Identifying potential beam-induced artefacts

In Sect. 5, we extensively discuss the general features detected in the ORGANIC images. To characterise the robustness of these features against dirty beam artefacts, we performed a simulation test using a mirrored version of the final ORGANIC images

(similar to e.g. Planquart et al. 2024). We extracted synthetic V2 and ϕ_3 observables from horizontally mirrored versions of the final ORGANIC images (Figs. 3 & 4), using the same (u, v) coverage (Fig. 1), imaging and SPARCO parameters (Table 3),

and observable uncertainties (Fig. E.1). Following the procedure outlined in Sect. 4.3.1, we then performed image reconstruction with ORGANIC on these synthetic observables. This procedure is equivalent to taking the final ORGANIC image as a 'model', and seeing how reliable the features of this model are recovered under reconstruction with a mirrored (u, v) coverage. Any general features (brightness enhancements, flux arcs, etc.) that re-

tain their integrity in the resulting mirror reconstructions – taking into account that the reconstruction induces additional blurring and stretching in the direction of the primary beam – are highly robust against changes in (u, v) coverage and hence dirty beam artefacts. Features that disappear are not reliable, as they are highly sensitive to the specifics of the (u, v) coverage, and hence likely affected by dirty beam artefacts.

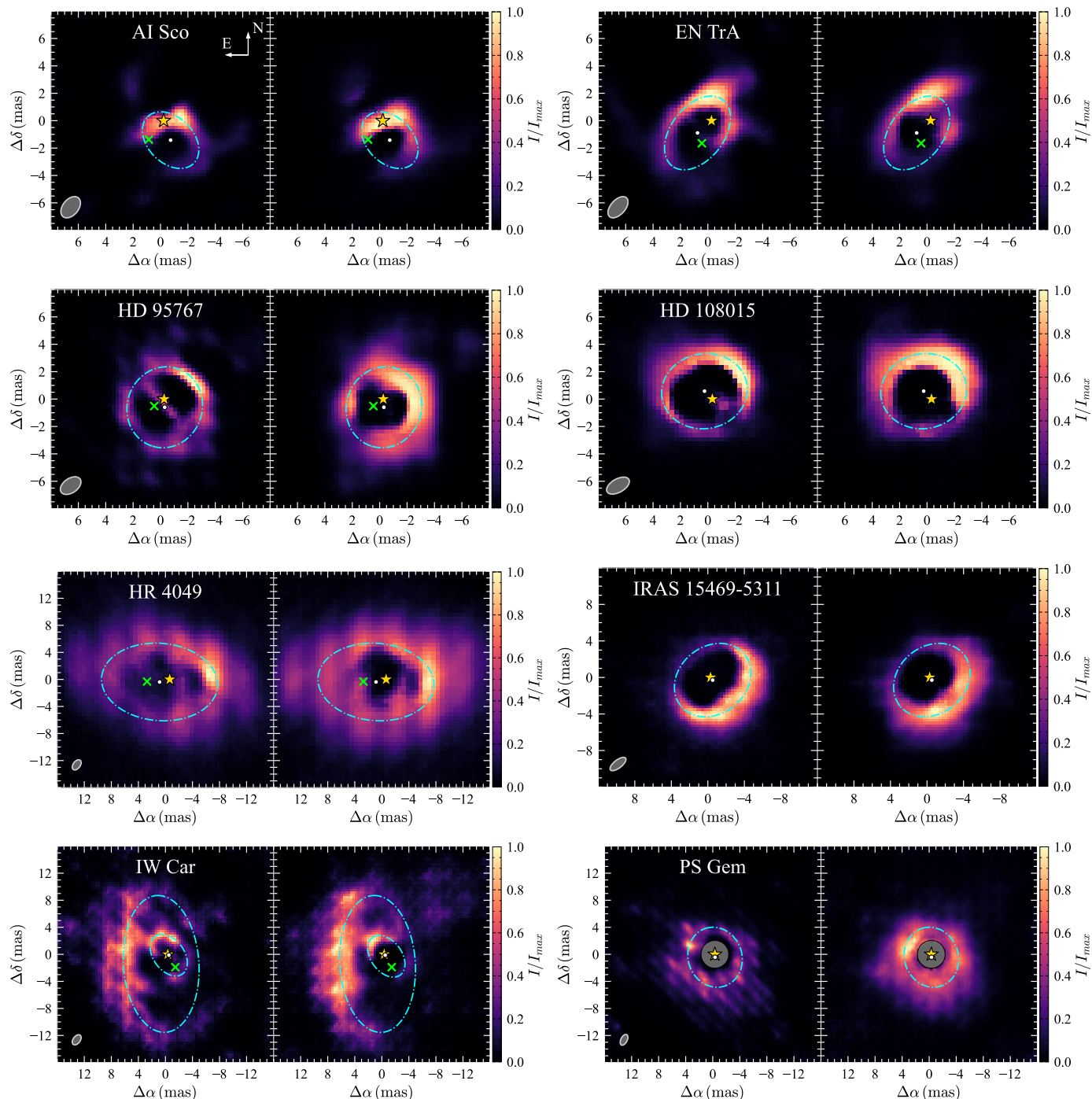


Fig. F.2: Mirrored final ORGANIC images (left-hand side) and their simulated image reconstructions from synthetic data (right-hand side). The displayed rim fits are mirrored versions of those derived from the ORGANIC images (Table 3). All symbols are otherwise analogous to Fig. 3.

We find the following for each of our targets:

AI Sco. We recover the expected strong brightness enhancement near the position of the primary star, shifted towards the projected rim's major axis.

EN TrA. We recover the expected strong brightness enhancement near the position of the binary star, shifted towards the projected rim's major axis.

HD 95767. The azimuthal brightness enhancement along the inner rim in the original image is heavily smeared out, and its contrast with the rest of the inner rim is heavily reduced. This indicates it is highly sensitive to the specifics of the (u, v) coverage. Similarly, the central bar of emission crossing the inner rim cavity is not recovered, indicating it is an artefact induced by the dirty beam. In fact, HD 95765 seems to be the most sensitive to dirty beam artefacts out of all targets. A likely culprit is the exceptionally high secondary flux fraction – $f_{\text{sec}} \sim 25\%$, while $f_{\text{sec}} \lesssim 5\%$ for the others (Table 3). This causes significant degeneracy between the secondary and the rim's azimuthal intensity profile with respect to the ϕ_3 data. Slight over- or underestimations in the secondary's SPARCO parameters can then cause significant dirty beam artefacts, despite the otherwise excellent (u, v) coverage (Fig. 1). The reconstructed mirror rim also widens substantially. While this is partly to be expected due to the mirror reconstruction introducing additional smearing, the effect is stronger than in the other targets, indicating that the excessive thinness of the rim at certain positions in the original image is unreliable. Due to these complications, reliable constraints on the rim morphology of HD 95767 will have to be derived from interferometric observations in longer wavelength bands (e.g. with VLTI/MATISSE), where the central stars' flux contributions are more diminished.

HD 108015. We recover the strong brightness enhancement shifted towards the projected rim's major axis. The small amount

of flux found inside the cavity close to the darkest spot along the rim (where the intensity approaches zero) is not recovered. Similarly, the dark spot is filled in. These two features are most probably dirty beam artefacts.

HR 4049. The strong brightness enhancement shifted toward the rim's major axis is recovered. The deep drop in brightness in the south-western part of the original image (south-eastern in the mirrored image) is partially filled in, indicating it was slightly affected by dirty beam artefacts. Similarly, a non-negligible amount of flux is pulled interior of the rim into the cavity in the mirror reconstruction, showing that the small amounts of flux found interior of the rim in the original image are unreliable.

IRAS 15469-5311. The generally smooth profile IRAS 15469-5311, largely symmetrically distributed around the rim's minor axis, is recovered.

IW Car. Both the large outer arc as well as the inner arcs closer to the central binary are generally recovered, indicating their robustness. The lower-significance flux feature immediately south of the secondary star is, however, not recovered, marking it as a potential artefact.

PS Gem. The general 'choppiness' of the rim has disappeared, and instead we recover a smoothed, smeared out version of the mirrored image. This is due to the fact that the secondary lobes of PS Gem are relatively anti-symmetric under horizontal mirroring (Fig. F.1). As a result, the choppy nature of the original reconstruction caused by dirty beam artefacts is mostly cancelled out by similar artefacts of the mirrored dirty beam. Interestingly, the bright spot towards the north-west in the original image (north-east in the mirrored image) is recovered up to a slight loss in contrast. Nevertheless, given that the imaged rim in general is heavily affected by artefacts (Sect. 5.3.8), we err on the side of caution, and do not consider it to be a reliable feature.